

Synergistic doping and stabilization of magnetically tunable $LnTi_3(Sb,Sn)_4$ ($Ln:Ce-Gd$) kagome metals

Brenden R. Ortiz,^{1,*} Ramakanta Chapai,^{1,2} German Samolyuk,¹ Milo Sprague,³ Arun K. Kumay,³ Hu Miao,¹ Karolina Górnicka,^{1,4} Xiaoping Wang,⁵ Qiang Zhang,⁵ Madhab Neupane,³ David Parker,¹ and Jiaqiang Yan¹

¹Materials Science and Technology Division, Oak Ridge National Laboratory, Oak Ridge, TN 37831, USA

²Department of Physics, Norfolk State University, Norfolk, VA 23504, USA

³Department of Physics, University of Central Florida, Orlando, FL 32816, USA

⁴Applied Physics and Mathematics Department, Advanced Materials Centre,

Gdansk University of Technology, ul. Narutowicza 11/12, 80-233 Gdansk, Poland

⁵Neutron Scattering Division, Oak Ridge National Laboratory, Oak Ridge, TN 37831, USA

(Dated: March 17, 2026)

Here we present our synthesis and characterization of the $LnTi_3(Sb,Sn)_4$ ($Ln: Ce, Pr, Nd, Sm, Gd$) family of cleavable kagome metals. While these materials are isostructural to the $LnTi_3Bi_4$ family, they only form as (Sb,Sn) solid-solutions with no corresponding $LnTi_3Sb_4$ or $LnTi_3Sn_4$ phases. We use a combination of first-principles density functional theory (DFT) and Crystal Orbital Hamilton Population (COHP) calculations to show that (Sb,Sn) alloying has a stabilizing effect on the structure by adjusting the Fermi level, filling bonding states, depopulating antibonding states, and adjusting the density-of-states (DOS) towards local minima, an effect we call “synergistic doping.” The tunable Fermi level also has a profound effect on the magnetism, which we demonstrate through a detailed characterization of the $SmTi_3(Sb,Sn)_4$ series. The series hosts multiple magnetic ground states resulting from competing magnetic interactions that are tunable by the (Sb,Sn) ratio. While the focus of this work is on $SmTi_3(Sb,Sn)_4$, we briefly comment on the (Sb,Sn) solubility range and the conferred magnetic tunability in the other rare-earths compounds ($Ln: Ce, Pr, Nd, Gd$) as well. Our work demonstrates how the (Sb,Sn) synergistic pair can be used to stabilize the $LnTi_3(Sb,Sn)_4$ structure while simultaneously providing a means to tune the magnetism, ultimately providing a potential route to develop new intermetallics with chemical, magnetic, and electronic tunability.

I. INTRODUCTION

Research into kagome intermetallics continues to represent a key intersection between fundamental condensed matter physics and solid-state chemistry. In particular, the search for materials that host complex magnetic and electronic instabilities has drawn significant attention to the distinctive band structure associated with kagome metals, which is known to generate a unique electronic structure replete with Dirac points, flat bands, and van Hove singularities. [1–3] Naturally, the kagome motif rarely exists in vacuum, and the applicability of these models depends heavily on the actual crystal structure and chemical composition. For example, we often study materials where the “contaminating” effect of other orbitals and supporting sublattices can be minimized, often by controlling the dimensionality of the compound.[4] Another crucial parameter that parametrizes a kagome compound is the alignment of the Fermi level with key features in the electronic structure. Thus, there are a wide array of chemical and structural considerations which must be made to enable the latent potential of the kagome motif in real materials.

Invigorated in part by our earlier discovery of the AV_3Sb_5 ($A: K, Rb, Cs$) kagome metals [5, 6], a huge body of research has emerged investigating emergent topolog-

ical, electronic, and magnetic instabilities (e.g. charge-density waves and superconductivity) within kagome metals.[7–13] Unfortunately, it seems that the chemical flexibility of the AM_3X_5 family is limited. Since the original discovery, only three other materials have been discovered: $CsCr_3Sb_5$ [14], $CsTi_3Bi_5$ [15], and $RbTi_3Bi_5$ [15]. This scarcity has helped ignite a wide range of exploratory studies searching for new kagome intermetallics exhibiting density-wave instabilities. Materials based in the extended CoSn-family (including AM_6X_6 materials) are the most topical examples, with recent discoveries of density-wave behavior exhibited in $LuNb_6Sn_6$,[16] ScV_6Sn_6 ,[17] and $FeGe$. [18] However, unlike the more electronically-driven behavior in the AM_3X_5 family, the CoSn-based derivatives appear to be driven by a combination of steric effects that affects only a small subset of the known compounds.[19–30]

Another rapidly developing family of cleavable kagome metals is the AM_3X_4 family. The AM_3X_4 materials contain two key structural motifs of interest: 1) zig-zag chains of A atoms, and 2) kagome nets formed by M ions. The A site is often occupied by electropositive rare-earth or alkali-earth metals, enabling a wide array of highly anisotropic, low-dimensional magnetic properties. Combined with the electronic structure imparted by the kagome network, these materials have a high potential for magnetic, electronic, and structural interactions. We previously reported on the discovery of the antimonide[31] LnV_3Sb_4 ($Ln: Eu^{2+}, Yb^{2+}$) and bismuthide[32, 33] $LnTi_3Bi_4$ ($Ln: La...Tb^{3+}, Eu^{2+}$,

* ortizbr@ornl.gov

Yb²⁺) kagome metals. These materials are part of a larger class of AM_3X_4 kagome metals reported in recent years.[5, 31, 33–38]

Even more recently, reports have emerged suggesting the emergence of spin- and charge-density anomalies in TbTi₃Bi₄,[39] GdTi₃Bi₄,[40] and CeTi₃Bi₄. [41] In the case of CeTi₃Bi₄, there is good evidence for a van Hove singularity-assisted spin-density wave, demonstrating the intertwining of magnetic and electronic interactions. Particularly within the bismides, the availability of large, cleavable single crystals has made the AM_3X_4 systems amenable to many experimental techniques. A number of angular-resolved photoemission (ARPES),[42–51] scanning-tunneling microscopy (STM),[40, 51] and other complementary techniques (e.g. magnetic force microscopy, torque magnetometry, and neutron diffraction)[51–53] have investigated the connection between the electronic structure and the rare-earth magnetism. Concomitant with the complex magnetic properties, a wide array of complex magnetotransport phenomena[32, 39, 54, 55] have been observed, including a record-large anomalous Hall effect (AHE) in TbTi₃Bi₄. [39] Particularly given the relative youth of the AM_3X_4 family, these materials appear to be a fertile ground for exploring the interaction between magnetism and the underlying kagome band structure.

This work focuses on the synthesis and characterization of an analogous series of materials, the $LnTi_3(Sb,Sn)_4$ (Ln : Ce–Gd) metals. These materials exist only as a solid-solution between the hypothetical $LnTi_3Sn_4$ and $LnTi_3Sb_4$. Accordingly, we first explore the stabilizing effect of the (Sb,Sn) alloying using a combination of density-functional theory (DFT) and crystal orbital Hamilton population (COHP) calculations. We demonstrate that the (Sb,Sn) pair electronically stabilizes the structure by controlling electron filling while not dramatically altering the electronic structure. We dub this effect “synergistic doping” and subsequently propose a synthetic strategy based on synergistic pairs. The variable Fermi level also manifests as tunable magnetism, which we demonstrate through a detailed investigation of the $SmTi_3(Sb,Sn)_4$ physical properties. We show that the system exhibits both ferromagnetic (FM) and antiferromagnetic (AFM) signatures, and that the (Sb,Sn) ratio can control the blending and dominance of the interactions. We also briefly comment on the (Sb,Sn) control and analogous properties in the other rare-earth (Ce, Pr, Nd, Gd) compounds as well. Our results ultimately show how the (Sb,Sn) synergistic dopants can stabilize the $LnTi_3(Sb,Sn)_4$ crystal structure, control the magnetic ground state, and provide a potentially new synthetic strategy for the discovery of complex intermetallic compounds.

II. METHODS

A. Synthesis

$LnTi_3(Sb,Sn)_4$ (Ln : Ce–Gd) single crystals are grown from alloys of (Sb,Sn) using the self-flux method. Rare-earth metal pieces (Ames) were placed with Ti powder (Alfa 99.9%), Sb shot (Alfa 99.999%), and Sn shot (Alfa 99.9%) into 2 mL Canfield crucibles fitted with a catch crucible and a porous frit.[56]. The ratio of Ln and Ti was fixed relative to the total amount of (Sb,Sn) flux such that the total composition adhered to $Ln_{0.25}Ti_{0.75}Sb_xSn_{10-x}$. The specific (Sb,Sn) flux compositions that yield single crystals is discussed later.

The filled crucibles were sealed under approximately 0.7 atm of argon gas in fused silica ampoules. Samples were heated to 1050°C at a rate of 200°C/hr and thermalized at 1050°C for 12 h. The vast majority of samples are cooled to 750°C at a rate of 2°C/hr. However, we observe that the most Sn-rich compositions often require further cooling to 650°C to form the correct phase. Excess (Sb,Sn) flux was removed through centrifugation at either 750°C or 650°C.

Single crystals of $LnTi_3(Sb,Sn)_4$ are silver-colored hexagonal plates with a metallic luster. Sample sizes commonly range from 1-10 mm depending on the rare-earth species and the specific ratio of (Sb,Sn). Unlike the structurally analogous $LnTi_3Bi_4$ compounds, $LnTi_3(Sb,Sn)_4$ are completely stable in air and atmospheric moisture. Samples have remained untarnished on the scale of 6 months, unlike the $LnTi_3Bi_4$ compounds which will tarnish and spall within a few hours in air. $LnTi_3(Sb,Sn)_4$ crystals retain their easy (00L) cleavage plane, and can be readily cleaved with a sharp blade. Cleaved surfaces can be further exfoliated using adhesive tape.

B. Bulk Characterization

Elemental analysis of single crystals was carried out on as-grown crystals using a Hitachi-TM3000 microscope equipped with a Bruker Quantax 70 EDS system. Crystals were mounted on carbon tape and cleaved to reveal pristine, flat surfaces before elemental analysis was performed. Subsequently, single crystals of $LnTi_3(Sb,Sn)_4$ were mounted on Kapton loops with Paratone oil for single crystal x-ray diffraction (SCXRD). Diffraction data were collected at 300 K on a Bruker D8 Advance Quest diffractometer with a graphite monochromator using Mo $K\alpha$ radiation ($\lambda = 0.71073$ Å). Data integration, reduction, and structure solution was performed using the Bruker APEX4 software package. As noted in previous manuscripts,[33, 35] SCXRD is a challenging endeavor on these materials due to their naturally large sizes, extremely soft mechanical properties, and exfoliable nature. Due to the difficulty of resolving Sb and Sn in X-ray diffraction, we also performed prelim-

inary neutron diffraction measurements on Sb-rich crystals of $\text{NdTi}_3(\text{Sb},\text{Sn})_4$ (295 K) on the TOPAZ beamline at the Spallation Neutron Source, Oak Ridge National Laboratory.[57] Within resolution of our measurement, we were not able to find significant evidence for preferential occupancy of (Sb,Sn), and no structural superlattices were observed.

Magnetization measurements (300 – 1.8 K) on crystals of $\text{LnTi}_3(\text{Sb},\text{Sn})_4$ were performed in a 7 T Quantum Design Magnetic Property Measurement System (MPMS3) SQUID magnetometer in vibrating-sample magnetometry (VSM) mode. Heat capacity measurements (300–1.8 K) were performed in a Quantum Design 9 T Dynacool Physical Property Measurement System (PPMS). Heat capacity measurements utilized the large-pulse (30% temperature rise) method, subsequently processed by both the dual-slope and single-slope method. Electronic transport measurements were performed in a Quantum Design 12 T Dynacool PPMS equipped with the Electronic Transport Option (ETO). An alternating current of 10 mA and 100 Hz frequency was applied as the probe current for magnetoresistance measurements.

C. Electronic Structure

Angle-resolved photoemission spectroscopy (ARPES) measurements were carried out at the Advanced Light Source (ALS) at Lawrence Berkeley National Laboratory. Data were collected at beamline 10.0.1.1 using a Scienta R4000 hemispherical electron analyzer with an incident photon energy of 60 eV. The angular and total energy resolutions were set to 0.2° and 15 meV, respectively. High-quality single crystals were cut and mounted on copper posts using silver epoxy, with ceramic posts affixed to the samples. After loading into the main chamber, the samples were cooled and maintained under vacuum for several hours, before cleaving the sample by striking the ceramic post. Sample cleavage and all subsequent measurements were performed at a sample temperature of 20 K under ultra-high vacuum conditions ($<10^{-10}$ Torr). Supplementary ARPES was performed at beamline 21-ID-1 of NSLS-II at Brookhaven National Lab (BNL) with an incident energy of 100 eV, linearly polarized photons, and 15 meV energy resolution.

DFT results utilized self-consistent methods[58] to evaluate the electronic structure of $\text{SmTi}_3(\text{Sb},\text{Sn})_4$. The electronic exchange correlations were incorporated using generalized gradient approximation (GGA) within the Perdew-Burke-Ernzerhof (PBE) [59] parametrization. The plane-wave basis projector augmented-wave approach (PAW) [60] as implemented in the Vienna Ab-initio Simulation Package (VASP) [61, 62] was used. We used a plane-wave energy cutoff of 450 eV and a $6 \times 6 \times 6$ k-point mesh to execute the self-consistent calculations. The Sm^{3+} pseudopotential describes electron ion interaction for Sm atoms and is accurate enough to describe details of the band structure in the nonmagnetic state.

For Ti, the pseudopotential used treats the 3p semicore states as valence states. The original structure atomic positions were optimized until the energy change was below 0.05 meV and forces were below 0.5 meV/Å.

For a chemical interpretation of the bonds within $\text{SmTi}_3(\text{Sb},\text{Sn})_4$, we employed the Crystal Orbital Hamilton Population (COHP) analysis. This technique allows us to represent the decomposition of the band structure over pair projected orbitals[63, 64] and ultimately allows us to identify bonding and antibonding contributions pairwise atomic interactions. The COHP calculations utilize our VASP results[65] as inputs to the LOBSTER COHP package.[66] Postprocessing of the LOBSTER results was performed using LOPOSTER.[67]

III. RESULTS AND DISCUSSION

A. Synthesis and Crystal Structure

Initial attempts to prepare the LnTi_3Sb_4 analogs of the LnTi_3Bi_4 phases[5, 33–38] via Sb self-flux were unsuccessful. However, using a Sn-based flux produced the structurally analogous $\text{LnTi}_3(\text{Sb},\text{Sn})_4$ (Ln : Ce–Gd) series of alloys. An abbreviated representation of the crystal structure is shown in Figure 1(a) and CIF files for a representative selection of the $\text{LnTi}_3(\text{Sb},\text{Sn})_4$ compounds is provided in the supplemental information. The structure has two sublattices of interest: 1) the Ln -based zig-zag chains, and 2) the Ti-based kagome network, both highlighted in Figure 1(b). Compared to the corresponding bismuthide, the unit cell shrinks approximately 7% (SmTi_3Bi_4 : 1500Å^3 , Sb-rich $\text{SmTi}_3(\text{Sb},\text{Sn})_4$: 1400Å^3), which is reflected in the associated Ti–Ti and Ln – Ln interatomic distances. Owing to the stronger Sb–Ti bonds, the $\text{LnTi}_3(\text{Sb},\text{Sn})_4$ appear to be stable in air and atmospheric water for up to a year without tarnishing, a dramatic improvement on the air-sensitive (<1 hr.) bismuthides.

As remarked before, the $\text{LnTi}_3(\text{Sb},\text{Sn})_4$ series appears to contain a substantial amount of (Sb,Sn) mixing, and we were unable to isolate either the pure antimonide or the pure stannide using flux methods. A prior report from Bie *et. al* also notes their inability to form either SmTi_3Sb_4 or NdTi_3Sb_4 using solid-state methods,[68] suggesting that these phases may not exist. Using (Sb,Sn) alloys as the flux, we prepared single crystals $\text{LnTi}_3(\text{Sb},\text{Sn})_4$ for the extended series from Ln : (Ce–Gd), and further identified the solubility range under a variety of (Sb,Sn) ratios and synthetic conditions.

Figure 1(c) summarizes the range of accessible (Sb,Sn) alloys for each of the rare-earth elements investigated here. The Sb-rich side of the diagram highlights that the compounds are nearly pure antimonides. Figure 1(d), which shows the nominal (Sb,Sn) flux composition against the actual (Sb,Sn) incorporation in the single crystals, further highlights the $\text{LnTi}_3(\text{Sb},\text{Sn})_4$ favoritism

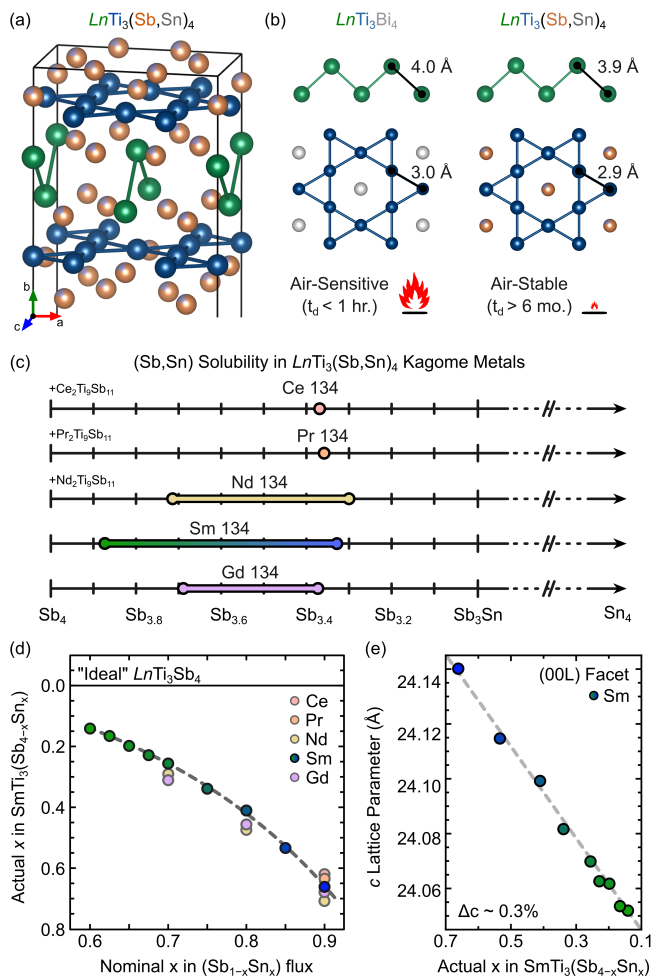


FIG. 1. (a) Abbreviated view of the $Fmmm$ $LnTi_3(Sb,Sn)_4$ crystal structure. (b) A schematic comparison of the structural motifs in the $LnTi_3Bi_4$ and $LnTi_3(Sb,Sn)_4$ families. (c) (Sb,Sn) solubility ranges for each of the flux-grown $LnTi_3(Sb,Sn)_4$ single crystals. We've also highlighted compositions where competition with $Ln_2Ti_9Sb_{11}$ phase is observed. (d) Processing diagram showing the incorporation of (Sb,Sn) into the crystal structure depending on the nominal Sb percentage in the flux. (e) Shift in the $SmTi_3(Sb,Sn)_4$ c -axis lattice parameter as a function of composition, derived from $\{00L\}$ facet scans.

towards Sb-rich compositions. Even at 10% nominal Sb loading in the flux, the (Sb,Sn) site is 80% Sb, though there are diminishing returns as more Sb is added to the flux. After 40-50% doping, even the Sm-containing series terminates with the appearance of other ternary and quaternary phases. We hypothesize that the reduced (Sb,Sn) solubility in the Ce and Pr compounds may be a consequence of a competing ternary antimonide $Ln_2Ti_9Sb_{11}$ (Ln : La–Nd) we reported previously.[69] This may also explain the absence of a La-containing $LnTi_3(Sb,Sn)_4$, as we previously showed that the competing $Ln_2Ti_9Sb_{11}$ is stabilized most by the larger La ion.

In standard lab X-ray diffraction (XRD), it is very difficult to distinguish Sb and Sn due to their negligible Z -

contrast. To check the distribution of (Sb,Sn) we performed a preliminary neutron diffraction experiment on crystals of $NdTi_3(Sb,Sn)_4$ and found no indications of a preferential distribution of (Sb,Sn). As an additional check against our energy dispersive spectroscopy (EDS) results, we performed (00L) facet scans on cleaved crystals of $SmTi_3(Sb,Sn)_4$ which provides a very accurate determination of the c -axis lattice parameter. Despite the similar size and chemistry of (Sb,Sn), we still expect a weak contraction of the unit cell as the Sb concentration increases. Figure 1(e) confirms the very weak (0.3% change) in the c -axis lattice parameter across the entire $SmTi_3(Sb,Sn)_4$ alloy series. For comparison, this effect is over an order-of-magnitude weaker than the volumetric change across the rare-earth series (3.5% between $CeTi_3(Sb,Sn)_4$ and $GdTi_3(Sb,Sn)_4$). The corresponding plot of the cell volume versus the 9-coordinate Shannon radius can be found in the supplementary information.

We see no evidence of peak splitting in facet scans and no compositional segregation in energy dispersive spectroscopy (EDS), indicating good structural homogeneity throughout the 1-5 mm sized crystals. Crystals within a single batch exhibit consistent stoichiometry and properties, and general batch-to-batch behavior can be well-reproduced. We have observed that altering the ratio of the starting reagents (e.g. $Ln_{0.25}Ti_{0.75}Sb_xSn_{10-x}$ vs $Ln_{0.25}Ti_{0.75}Sb_{2x}Sn_{20-2x}$) will change the correspondence of actual:nominal, but will not enable further incorporation of Sb in the $LnTi_3(Sb,Sn)_4$ series. From the uniform expansion of the unit cell, the lack of peak splitting, the uniform spectroscopy results, and our synthetic observations, we believe that the crystals are macroscopically homogeneous alloys. There is always the potential for short-range (Sb,Sn) fluctuations, however, and more detailed measurement techniques (e.g. MFM or STM) could be interesting routes to investigate the local effect of the (Sb,Sn) doping on the electronic and magnetic properties.

For the remainder of this manuscript we will focus on the $SmTi_3(Sb,Sn)_4$ series. We choose $SmTi_3(Sb,Sn)_4$ because it shows the largest variation in (Sb,Sn) incorporation, exhibits a strong and complex magnetic ground state with a relatively high transition temperature (10-20 K), and exhibits anisotropy (easy c -axis) which is easily oriented for. Throughout the paper we will refer to the Sb-rich terminus of the Sb-series ($SmTi_3Sb_{3.86}Sn_{0.14}$) simply as Sb-rich $SmTi_3(Sb,Sn)_4$, and it will be colored green in all subsequent plots. Similarly, the Sn-rich composition ($SmTi_3Sb_{3.34}Sn_{0.66}$) will be referred to as Sn-rich $SmTi_3(Sb,Sn)_4$ and will be colored blue. A brief discussion of the other rare-earth elements $LnTi_3(Sb,Sn)_4$ (Ln : (Ce,Pr,Nd,Gd)) is included at the end of the manuscript with basic characterization data included in the supplementary information.

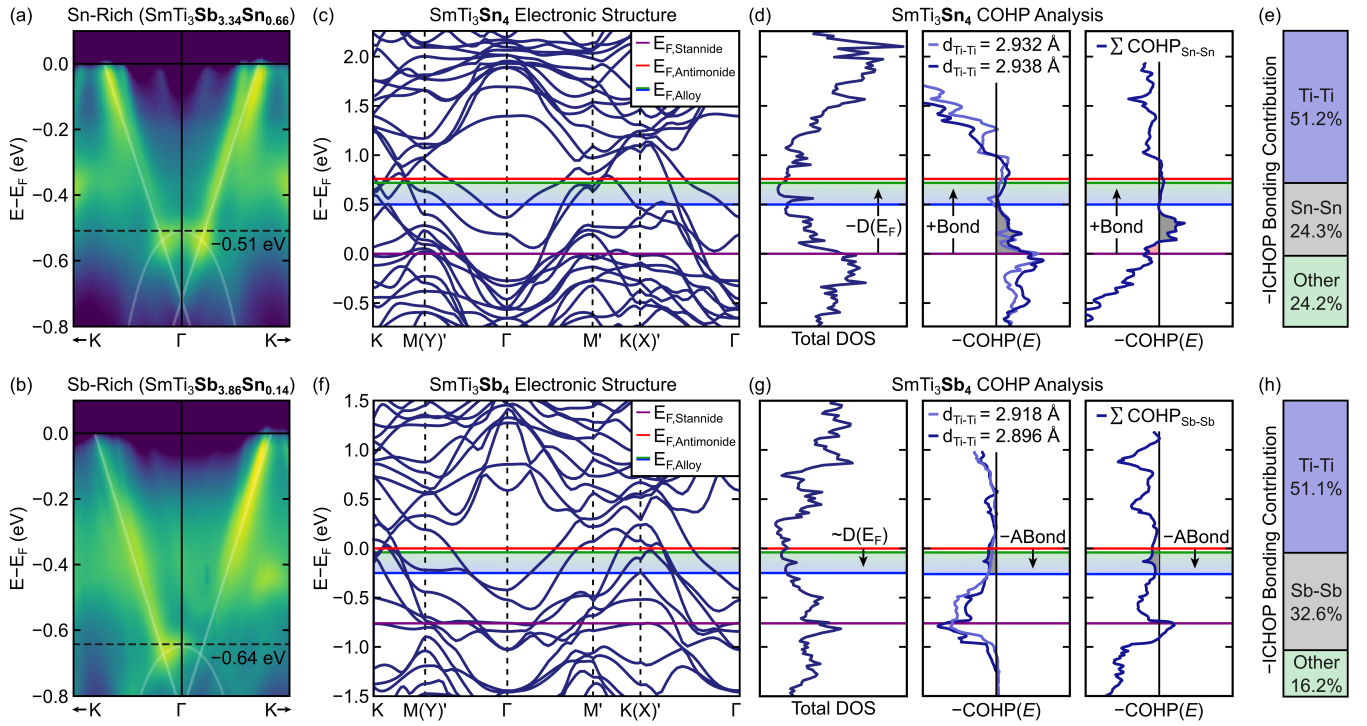


FIG. 2. (a) Experimental ARPES data for a Sn-rich $\text{SmTi}_3(\text{Sb},\text{Sn})_4$ crystal, with several bands highlighted in white. Note the concave-down band approximately 0.5 eV below E_F . (b) Analogous ARPES data for a Sb-rich $\text{SmTi}_3(\text{Sb},\text{Sn})_4$ crystal. The concave-down band is now 0.64 eV below E_F , indicating an effective doping of approximately 270 meV per Sb/Sn atom. (c) Electronic band structure for the hypothetical SmTi_3Sn_4 . Several values of E_F are shown: the native stannide (purple), the native antimonide (red), and the range approximating the alloying range (green/blue). (d) Density of states ($D(E)$) and Crystal Orbital Hamilton Population (COHP) calculations for SmTi_3Sn_4 showing that electron doping (Sb-substitution) in the stannide is favorable through reduction of $D(E_F)$ and population of additional bonding states. (e) Breakdown of integrated (ICOHP) contribution to the total bonding band energy for Ti-Ti and Sn-Sn (shown) relative to all other atom pairs. (f) Dispersion for hypothetical SmTi_3Sb_4 shown with same set of E_F as before. (g) Analogous $D(E)$ and COHP calculations for the antimonide. Hole doping (Sn-substitution) in antimonide is favorable through reduction of antibonding states at E_F while maintaining low $D(E_F)$. (h) Breakdown of integrated ICOHP contribution for antimonide.

B. “Synergistic Doping” and Stability of $\text{LnTi}_3(\text{Sb},\text{Sn})_4$

Both our work and work from Bie et. al[68] suggest that the $\text{LnTi}_3(\text{Sb},\text{Sn})_4$ compounds exist only as an alloy between the hypothetical compounds LnTi_3Sb_4 and LnTi_3Sn_4 . We hypothesize that the structure may be stabilized by a certain electron count, and that the chemical (radii, electronegativity, bonding) similarity of Sb and Sn allows the system to naturally equilibrate at the electron count that stabilizes the structure. For brevity, we are calling this effect – imbuing a system with chemically similar alloying agents to enable a natural charge degree-of-freedom and stabilize a structure – “synergistic doping.” In this section we will combine experimental angular-resolved photoemission spectroscopy (ARPES) and first-principles density functional theory (DFT) to examine whether a potential charge degree-of-freedom may explain the stabilization of the $\text{LnTi}_3(\text{Sb},\text{Sn})_4$ series. As mentioned before, we will focus on the Sm-containing series for the remainder of the discussion.

First, we establish that (Sb,Sn) enables tunability of

the Fermi level (E_F) in $\text{SmTi}_3(\text{Sb},\text{Sn})_4$ without drastically changing the electronic structure. To benchmark changes in E_F induced by the alloying, we performed experimental ARPES measurements on the Sn-rich ($\text{SmTi}_3\text{Sb}_{3.34}\text{Sn}_{0.66}$) and Sb-rich ($\text{SmTi}_3\text{Sb}_{3.86}\text{Sn}_{0.14}$) single crystals. These results are shown in Figure 2(a) and Figure 2(b), respectively. To determine the doping shift of E_F , we examine the intersection of a series of dispersive bands crossing through Γ with another concave-down band. The bands have been highlighted in the figure with a light gray trace and the intersection has been marked with a dashed black line. Subtracting the intersection energy in the Sn-rich data (-0.51 eV) from the Sb-rich data (-0.64 eV) yields a shift of 130 meV. Normalizing this shift to the (per atom) concentration difference between $\text{SmTi}_3\text{Sb}_{3.34}\text{Sn}_{0.66}$ and $\text{SmTi}_3\text{Sb}_{3.86}\text{Sn}_{0.14}$, we observe a shift of 260 meV per (Sb,Sn) substitution.

A similar experiment can be performed with DFT, where we simulate the expected shift in E_F under the effect of (Sb,Sn) doping. We will investigate the effect of Sb-doping on SmTi_3Sn_4 and Sn-doping on SmTi_3Sb_4 .

While these compounds do not formally exist, this alleviates the complexity of alloy simulations in low-symmetry, large unit cell systems and further lets us examine the differences between the electronic structures. Figure 2(c,f) show the DFT calculations for SmTi_3Sn_4 and SmTi_3Sb_4 over the pseudo-hexagonal Brillouin zone (for details on the pseudo-hexagonal zone projection, see our discussions in Ref [33, 41]). For each simulation we show three key values of E_F : (1) the native E_F for the pure Stannide (purple), (2) the native E_F for the pure antimonide (red), and (3) a range of potential E_F given the (Sb,Sn) alloying (blue/green). To determine the E_F window for the alloys, we used the compositions $\text{SmTi}_3\text{Sb}_{3.1}\text{Sn}_{0.9}$ and Sb-rich $\text{SmTi}_3\text{Sb}_{3.9}\text{Sn}_{0.1}$ and assumed that each (Sb,Sn) substitution results in 1 electron/hole per swap. This restraint yields a computed E_F window of 210 meV (a per atom basis of 263 meV per swap) which is in excellent agreement with experimental ARPES data.

The DFT results in Figure 2(c,f) also allow us to examine the general influence of (Sb,Sn) alloying on the bulk band structure. Qualitatively, the band structures of SmTi_3Sn_4 and SmTi_3Sb_4 are remarkably similar near the relevant E_F , despite full substitution of Sb and Sn. This suggests that the (Sb,Sn) swapping likely has a minimal impact on the local electronic structure, particularly near E_F . This is perhaps expected, since many kagome materials tend to have the states at E_F dominated by the M_3 atoms. In the supplemental information we have included a series of additional ARPES measurements that show further evidence for the innocuous nature of the (Sb,Sn) substitution. In short, we’ve observed that constant-energy-contours (CEC’s) generated around -130 meV in the Sb-rich compound (corresponding to the proposed doping level) produce CEC’s which are very similar to the CEC for the Sn-rich compound at its natural E_F . From these results, we believe that the alloying does not impact the bulk electronic structure in any substantial manner and primarily acts to tune E_F .

We’re now prepared to tackle *why* the $\text{LnTi}_3(\text{Sb,Sn})_4$ compounds are stabilized by Fermi level tuning. For this discussion we will combine density of states ($D(E)$) calculations and Crystal Orbital Hamilton Population (COHP) to provide a qualitative argument for the enhanced stability of the alloys. Prefacing our discussion, we intuitively expect that materials *generally* crystallize such that E_F is placed near a local minimum in $D(E)$. While not a strict rule, placing E_F in such a way tends to reduce the system’s total energy. Systems with E_F at local maxima tend to distort or destabilize in a way that restructures the DOS and avoids high $D(E_F)$. However, $D(E)$ only provides the number of states and not the chemical character (e.g. bonding or antibonding) of the orbitals. For this we turn to COHP simulations, which allow us to identify specific bonding, antibonding, and nonbonding contributions to the electronic structure. In the typical presentation, COHP is presented as (-COHP(E)) where positive values

correspond to bonding states. Note that our discussion doesn’t include any arguments from configurational entropy, although those would generally be believed to enhance the energetic stability of an alloy as well.

Figure 2(d) presents $D(E)$ and COHP(E) calculations for SmTi_3Sn_4 . For clarity our discussion here will focus on the Ti–Ti and Sn–Sn interactions. These are two largest contributors to the total off-site bonding interactions (Figure S3(e,h) provide the relative contributions to the COHP), though all interactions are provided in the supplementary information. There are two unique Ti–Ti bond distances shown in Figure S3(d), though we have summed the nine individual Sn–Sn interactions for graphical clarity. From $D(E)$, we can see that the native Fermi level (purple) is near a local maximum in $D(E)$. Electron doping *via* Sb substitution (purple to green/blue) adjusts E_F up and into a local minimum. Furthermore, electron doping fills additional bonding states (shaded gray) in both the Ti–Ti and Sn–Sn COHP calculations, which further stabilizes the structure. The system reaches a natural limit in the electron-doped regime as further doping would increase $D(E_F)$ and incorporate substantial antibonding contributions.

An analogous effect can be observed in the antimonide. However, since the alloy range is very close to the antimonide limit, the effect is appreciably more subtle. Figure 2(g) examines the DOS and COHP simulations for SmTi_3Sb_4 near the relevant energies. Unlike the stannide, the antimonide already sits near a relatively flat local minimum in $D(E)$. Examining the dominant Ti–Ti and Sb–Sb COHP contributions reveals that the natural Fermi level in the antimonide naturally falls in a heavily antibonding regime. The antimonide feels two competing effects: the desire to keep $D(E)$ low, and the desire to depopulate antibonding states by pushing E_F down. The interplay between these two effects culminates as justification for the alloying range (green/blue) sitting slightly below the antimonide’s natural E_F (red). The system likely naturally self-limits the Sn doping due to increasingly large $D(E_F)$ under hole doping, even though the driving force to continue depopulating the antibonding states remains.

From our analysis, it seems plausible that the charge degree-of-freedom offered by the (Sb,Sn) pair may justify the formation of the $\text{LnTi}_3(\text{Sb,Sn})_4$ alloying series and the apparent difficulty in synthesizing the pure antimonide. We’ve demonstrated that (Sb,Sn) alloys substitute with nearly 1:1 doping efficiency, shifting the experimental Fermi level in accordance with simulations while leaving the bulk band structure largely unchanged near E_F . This combination of effects imbues the system with the charge flexibility needed to adjust the Fermi level, balancing energetic considerations from both the DOS and the bonding/antibonding COHP analysis. Employing the strategy of “synergistic doping” may have considerable implications on the discovery and development of other structurally complex intermetallics.

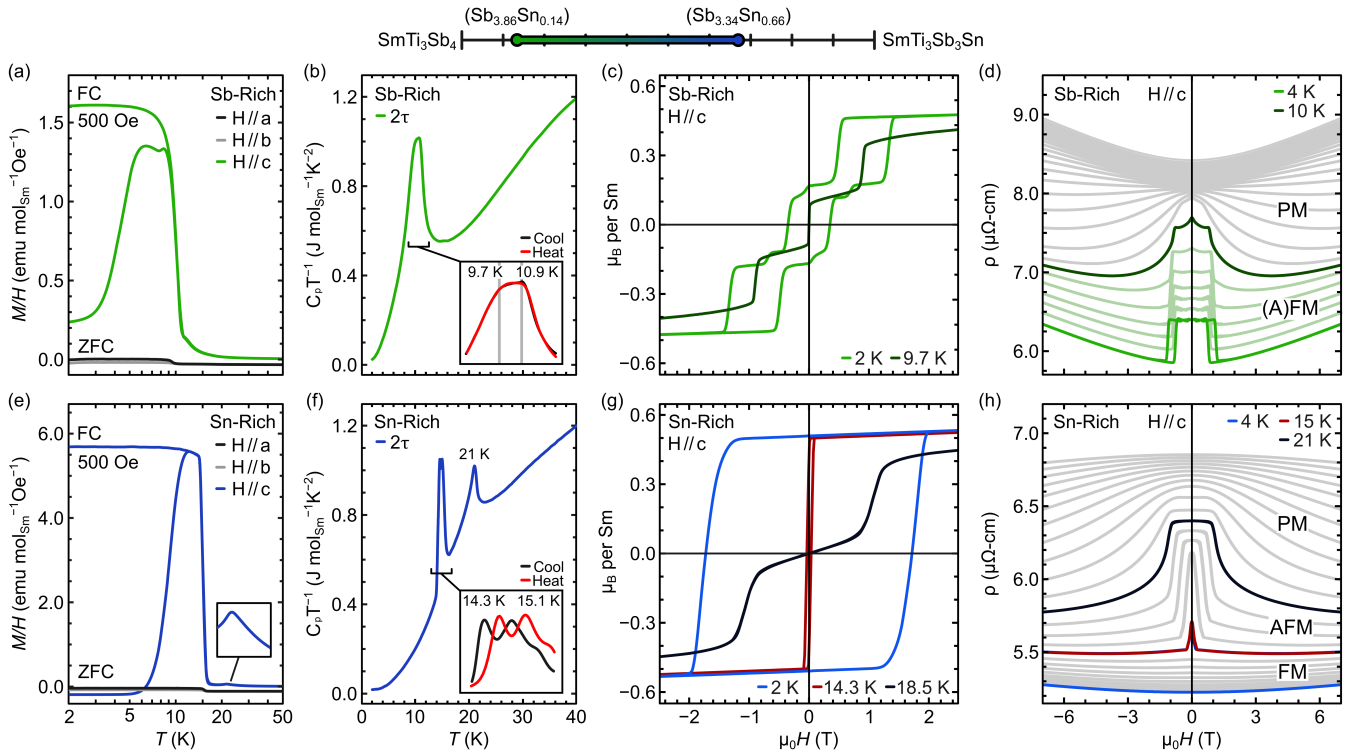


FIG. 3. Here we present the basic properties of the Sb-rich (green) and Sn-rich (blue) termini of the $\text{SmTi}_3(\text{Sb},\text{Sn})_4$ solid solution. (a,e) Field-cooled magnetization along three principle crystallographic directions, showing easy c -axis magnetization. Both systems show a higher-temperature cusp followed by a lower-temperature magnetization rise and plateau. (b,f) Large-pulse zero-field heat capacity measurements showing the multiple transitions in both compositions. Sn-rich samples show a second order peak at 21 K followed by a split first-order peak at 15 K. Sb-rich samples instead show a set of two second-order peaks at 9.7 K and 10.9 K. (c,g) Isothermal magnetization results with $H\parallel c$ clearly demonstrate the FM nature of the Sn-rich sample and the more complex A(FM) interactions in the Sb-rich endpoint. (d,h) Magnetoresistance measurements showing the emergence of negative magnetoresistance (MR) in the AFM state, which persists through 4 K in the Sb-rich sample. The onset of stronger FM order in the Sn-rich sample suppresses the AFM and the negative MR, consistent with the first-order nature of the AFM to FM transition Sn-rich heat capacity.

C. Properties of $\text{SmTi}_3(\text{Sb},\text{Sn})_4$ solid solution

The potential for kagome materials to host a suite of complex magnetic and electronic phases is well documented,[1–4] though the intentional alignment of the Fermi level with the purported features in the band diagram has always been a challenging task. The synergistic doping of $\text{LnTi}_3(\text{Sb},\text{Sn})_4$ is an excellent example of how control over electron filling can not only stabilize a crystal structure, but also provide a natural means to tune E_F . Further, given the strong magnetic character of the broader AM_3X_4 family, the (Sb,Sn) flexibility may provide a convenient means to investigate the impact of electron tuning on the magnetic and electronic properties.

Figure 3 presents a summary of the magnetic, electronic, and thermodynamic properties for the Sn-rich and Sb-rich endpoints of the $\text{SmTi}_3(\text{Sb},\text{Sn})_4$ series. We begin our discussion by focusing on the Sb-rich compound (green). Figure 3(a) demonstrates the field-cooled (FC) and zero-field-cooled (ZFC) magnetization

curves for a single crystal with the field oriented parallel to the three principle axes. $\text{SmTi}_3(\text{Sb},\text{Sn})_4$ exhibits a highly anisotropic magnetic response with a clear easy c -axis magnetization. Qualitatively the magnetization resembles a ferromagnetic (FM) system, replete with FC/ZFC splitting. However, a weak shoulder can be observed immediately before onset of the ferromagnetic response, the purported FM transition is broader than normally expected, and the plateau of approximately 1.5 emu/mol/Oe is fairly weak.

Heat capacity measurements (Figure 3(b)) indicate a somewhat broad second-order peak which coincides with the magnetization onset around 10 K. Closer analysis of the heat capacity peak clearly indicates two transitions separated by <1 K (see inset). The centroids of these peaks correspond to the weak shoulder and ZFC/FC splitting temperature in the magnetization results. Due to the lack of a non-magnetic standard in this system (we were unable to make either $\text{LaTi}_3(\text{Sb},\text{Sn})_4$ or $\text{CaTi}_3(\text{Sb},\text{Sn})_4$) we do not have a quantitative analysis of the magnetic entropy released, though a conservative estimate using a

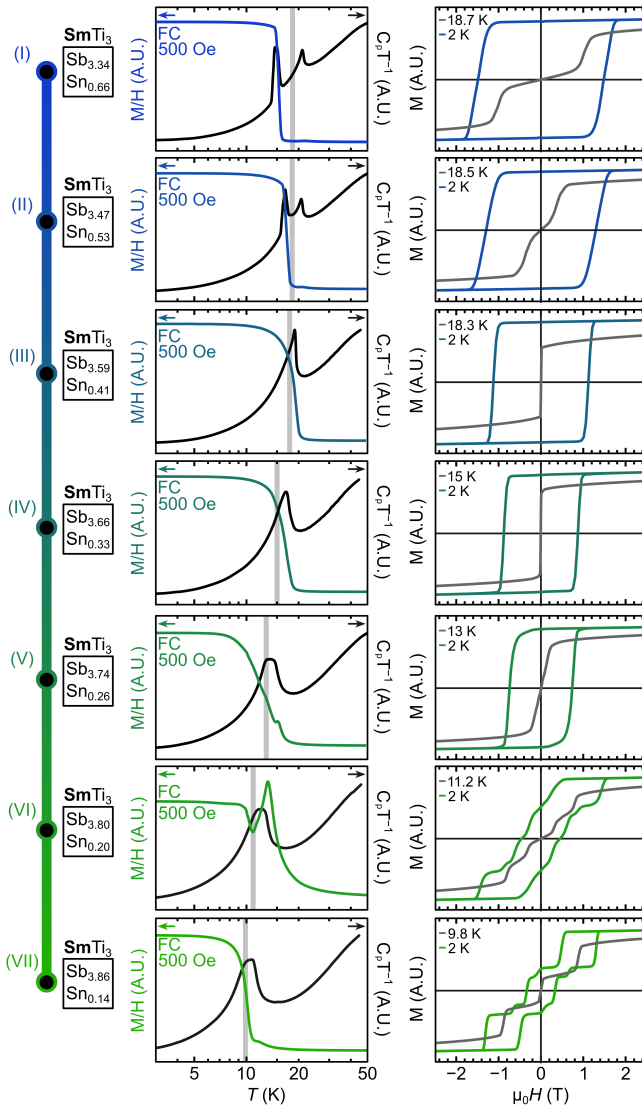


FIG. 4. Here we present a full series of samples traversing the $\text{SmTi}_3(\text{Sb},\text{Sn})_4$ solid-solution to demonstrate the gradual shift in magnetic and thermodynamic properties. Shown from left to right are: (1) the measured (Sb,Sn) content of the single crystals, (2) a plot showing the temperature-dependent magnetization and zero-field heat capacity results superimposed and scaled in arbitrary units, and (3) the corresponding isothermal magnetization curves at base temperature and an intermediate temperature (gray) intended to demarcate the transition between the two heat capacity features (where possible). For clarity, the intermediate temperature (gray) is also marked on the temperature-dependent magnetization.

simple polynomial subtraction estimates 80% of $\text{Rln}(2)$, which is consistent with the prior results for magnetic Sm^{3+} in the SmTi_3Bi_4 bismuthide.[33]

The coincidence of the split heat capacity peak and the magnetization features suggests that there are potentially two closely-interacting magnetic transitions. To investigate, we performed field-dependent magnetization measurements at two temperatures: (1) the base tem-

perature of 2 K, and (2) an intermediate temperature of 9.7 K (immediately before the onset of ZFC/FC splitting). At 9.7 K, Figure 3(c) reveals clearly antiferromagnetic (AFM) behavior with multiple spin-flip transitions. Upon cooling to 2 K, however, the system develops substantial coercivity. Together these effects explain both the weak peak (AFM cusp) and plateau (coercivity) in the temperature-dependent magnetization Figure 3(a). This effect is also observed in the symmetrized, transverse magnetoresistance (Figure 3(d)), where we can observe the sharp onset of negative MR with a critical field that matches the second spin-flop transition around 0.9 T. As the system continues to cool we observe the evolution of the same hysteresis observed in the magnetization results.

We now turn to the Sn-rich endpoint. As established in the ARPES and DFT data, these compositions differ by approximately 0.5 Sn per formula unit (or approximately 0.5 holes per formula unit), with only a very weak (0.3% change) response in the crystallographic parameters and minimal changes to the electronic structure. We anticipate that modifications to the magnetic ground state are primarily induced by changes in the electronic filling due to the synergistic doping effect. Figure 3(e) presents the ZFC/FC magnetization results, again highlighting a highly anisotropic FM response with easy *c*-axis magnetization. The Sn-rich compound exhibits a much sharper ferromagnetic onset and a plateau more in accordance with a prototypical FM. The broad peak from the Sb-rich compound reappears in the Sn-rich composition as well, though the separation is greater (≈ 6 K above) and the cusp shape is much clearer. Naively, these results suggest an AFM ground state from approximately 15–20 K before the AFM state is overtaken by a stronger FM state.

Heat capacity measurements (Figure 3(f)) clearly show two distinct thermodynamic signatures corresponding to the AFM and FM transitions. The AFM transition (21 K) is second-order, but the AFM to FM peak (15 K) is clearly first-order in nature. The inset of Figure 3(f) demonstrates the clear temperature splitting of the heating and cooling curves as measured by high-pulse single-slope heat capacity measurements. Isothermal magnetization measurements performed at temperatures between the two heat capacity peaks (Figure 3(g)) confirms the onset of AFM order below 21 K, suppression of the AFM order by 18.5 K, and emergence of strong FM behavior by 2 K. Note that the saturation magnetization is not modified substantially between the Sb-rich and Sn-rich compositions, suggesting that the (Sb,Sn) is modifying the magnetic interactions, but not the effective moment or Crystalline Electric Fields (CEF) of the Sm ion.

The electronic transport data for the Sn-rich composition (Figure 3(h)) supports a similar interpretation of the data. As we cool from the paramagnetic state into the antiferromagnetic state, we see the Sn-rich sample begin to exhibit a similar negative magnetoresistance as in the Sb-rich sample. However, instead of the negative

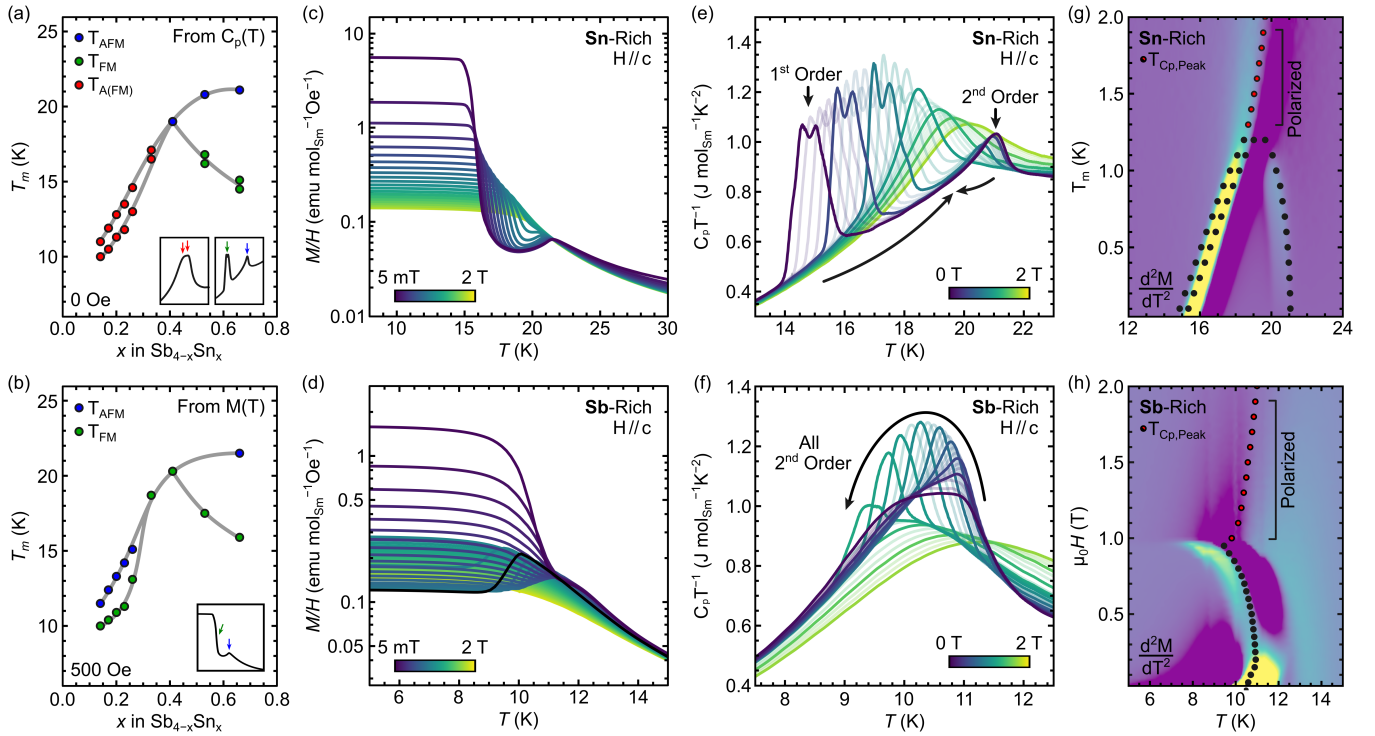


FIG. 5. Here we summarize the temperature-composition phase diagrams for the $\text{SmTi}_3(\text{Sb,Sn})_4$ solid-solution, and further investigate the field-temperature phase diagrams for the Sb-rich and Sn-rich termini of the alloys. Temperature-composition phase diagrams derived from (a) heat capacity and (b) magnetization measurements demonstrate the competition between the higher-temperature AFM order and the onset of FM order at lower temperatures. For Sb-rich compositions, the AFM order and FM interactions intertwine into the A(FM) state. (c,d) Temperature-dependent magnetization curves for the Sn-rich and Sb-rich termini at under various magnetic fields. The AFM-like cusp in the Sn-rich sample is evident and appears gradually suppressed under applied field. The AFM-like cusp in the Sb-rich sample is more subtle at low fields, but is strengthened and more dominant at intermediate fields (highlighted in black for clarity). (e,f) Field-dependent large-pulse heat capacity measurements to help visualize the multiple heat capacity peaks and their interplay with fields. (g,h) Composite plots where the gradient background is the second-derivative of the field- and temperature-dependent magnetization. Solid points are identified from the field- and temperature-dependent heat capacity results.

magneto-resistance developing the coercivity seen in the hybridized AFM/FM ground state of the Sb-rich (green) data, the Sn-rich sample (blue) shows the negative magneto-resistance vanish at the lower temperature phase transition. Furthermore, the critical field for the spin-flip transition visibly decreases as we continue cooling within the AFM state before fully disappearing in the FM states. This is strong evidence for the competition between AFM and FM states. Further, since the FM and AFM orders break different symmetries with different ordering vectors, the transition has to be first order (consistent with heat capacity results) since there is no symmetry allowed continuous route for this transition.

Let's broadly compare the Sb-rich and Sn-rich compositions. The Sn-rich (blue) composition exhibits a competition between AFM and FM order. The AFM order emerges first but is ultimately suppressed and replaced by the FM order. Contrast this with the Sb-rich (green) composition. After emergence of AFM order around 10-11 K, continued cooling sees substantial FM-like interactions emerge, indicated by both the irreversibility (coer-

civity) of the magnetization loops and the transport data. At this time, we suspect that the ground state of the system is likely either (1) AFM with substantial spin canting, (2) a ferrimagnet, or (3) AFM with evolution of a spin-density wave. At this time we have insufficient data to definitively characterize the magnetic nature of the Sb-rich $\text{SmTi}_3(\text{Sb,Sn})_4$. For brevity we will refer to this state as an A(FM) to represent the interplay between the AFM character and the clear coercivity (FM interactions). Although both the Sb-rich and Sn-rich samples show both AFM and FM character at some point, we find it remarkable that (Sb,Sn) not only tunes the interaction strength, but also fundamentally changes the nature of the interaction. The Sb-rich compound shows a more seamless blending of the AFM and FM states into the A(FM) state, whereas the Sn-rich data shows a more stark competition (e.g. first order AFM to FM) between energy scales.

Thus far we have only shown the Sb-rich and Sn-rich termini of the $\text{SmTi}_3(\text{Sb,Sn})_4$ solid solution, however, seeing the evolution of the magnetic and thermodynamic properties as a function of composition further

illustrates the interplay between the FM and AFM states. Figure 4 shows a series of $\text{SmTi}_3(\text{Sb},\text{Sn})_4$ single crystals ranging between the Sb-rich and Sn-rich termini. From left to right, we display (1) the explicit (Sb,Sn) compositions as determined by energy dispersive spectroscopy (EDS), (2) temperature-dependent magnetization superimposed with zero-field heat capacity results, and (3) isothermal magnetization curves at base temperature (color) and an intermediate temperature (gray) that straddles the AFM and FM transitions. For graphical simplicity, all results are shown in arbitrarily scaled units, though a corresponding set of quantitative plots is provided in the supplemental information.

Starting at the Sn-rich composition (Sample-I), we see the same highly coercive ferromagnetic loop and intermediate AFM-like state from Figure 3(g). As additional Sb is incorporated into the structure, the heat capacity peaks begin to merge and the temperature-dependent magnetization loses the characteristic “sharpness” of the FM transition (e.g. Sample-III). Note that by Sample-III and Sample-IV, we can no longer identify a temperature where the intermediate temperature traces (gray) exhibit intermediate spin-flip plateaus. By Sample-V, the 2 K FM loop develops a characteristic rounding and the intermediate temperature begins to redevelop the spin-flip plateau. This is most evident as we transition from Sample-V to Sample-VI, where the 2 K loop fractures into the individual plateaus and shows clear blending of the AFM and FM states. By sample-VII the hybrid A(FM) state is clearly developed and the individual plateaus are sharp and well-defined. Together, these results clearly demonstrate that both temperature and composition (electron filling) tuning can be used to smoothly tune the system between the AFM, FM, and (A)FM states.

Figure 5(a) and (b) provide the temperature-composition phase diagram for $\text{SmTi}_3(\text{Sb},\text{Sn})_4$ as derived from heat capacity and magnetization measurements. Heat capacity measurements (a) are likely the most detailed, as our high-pulse measurements can help identify both peak splittings and the difference between first- and second-order transitions. The inset helps indicate the color scheme for the samples, with the blue peaks indicating the highest (AFM) peak, and the green peaks indicating the lower-temperature first-order (FM) peaks. As demonstrated in Figure 3(a, inset), the first-order peak always appears as a split peak with at least two distinct peaks. Both of the peak temperatures are highlighted on the plot. Similarly, after the initial peak merger shown in Figure 4(Sample-III), the heat capacity peak broadens into a peak with a clear shoulder. While these peaks move together, they are distinct (as will be seen in the field-dependence shortly) and are marked as such here.

The magnetization results can be slightly harder to interpret, largely because the strength of the FM transition often obscures the AFM cusp. Unfortunately, due to the myriad of other features that also emerge in the interme-

mediate composition regime (recall Sample-V and Sample-VI from Figure 4), using the temperature-derivative is also a challenging task. The inset of Figure 5(b) shows a small log-scale schematic of the two features which are present in almost all temperature-dependent magnetization measurements. There is commonly a small, weak cusp at higher temperatures (consistent with the AFM heat capacity peak) and then the much stronger FM transition. If we define T_{AFM} as the cusp peak from the AFM transition and T_{FM} as the midpoint of the FM transition, then we can generate the magnetization-derived phase diagram shown in Figure 5(b). Both Figure 5(a) and Figure 5(b) agree qualitatively and quantitatively on the boundaries in the composition-temperature space.

Figure 5(c-h) turn to examine the field-dependence of the Sb-rich and Sn-rich endpoints. This is particularly instructive when examining the heat capacity results, as we can clearly see the multiple peak structure of the results. As with the composition-temperature phase diagram, we will examine both the magnetization and heat capacity results to help provide a more exhaustive interpretation of the results. Figure 5(c,d) examine the field-dependence of the magnetization curves on a logarithmic scale. For the Sn-rich sample (c) The higher-temperature AFM feature is clearly visible for a relatively wide range of fields, though it is progressively suppressed with the application of fields. For the Sb-rich sample (d) the situation is a bit more complex. At low fields there is a clear shoulder at higher temperatures (≈ 12 K) indicative of the onset of AFM-dominated interactions. However, unlike the Sn-rich sample, the application of a higher magnetic field doesn't progressively suppress the AFM interaction. Instead, there is an intermediate regime (note the black curve) where the AFM-like cusp is the dominant feature in the magnetization. This is consistent with the step-like features in the Sb-rich magnetization from Figure 3(c), as we know that intermediate fields at approximately 10 K should be consistent with a magnetization response that resembles a prototypical spin-flop AFM.

The heat-capacity curves are perhaps the most useful way to exhibit the interplay between the FM and AFM interactions in the system. Figure 5(e) shows the field-dependent ($H||c$) heat capacity results for the Sn-rich terminus. The purple (zero-field) curve clearly shows the split first-order peak and the higher-temperature AFM-like second-order peak. We've shown the series of field-dependent measurements with every 5th curve highlighted for clarity. At small to moderate fields (0-1 T) the first-order FM peak is affected the most, shifting towards higher temperatures while the AFM peak is only slightly broadened/shifted to lower temperatures. Above 1 T the AFM peak is rapidly suppressed and shifted downwards, merging into the first-order peak, which has also broadened enough to lose the double peak structure. As suggested by all previous measurements, this indicates that the Sn-rich sample exhibits a higher-temperature AFM which competes (and loses) to a FM-dominated ground

state.

Now we turn to the more complex Sb-rich $\text{SmTi}_3(\text{Sb,Sn})_4$ field-dependent heat capacity in Figure 5(f). The zero-field (purple) curve is clearly broad, with a clear right and left shoulder. With small applied fields (up to about 0.2 T) the centroid of the peak shifts towards higher temperatures (FM-dominant), the right shoulder sharpens into a well-defined peak, and the left shoulder is suppressed/merged. Above 0.2 T the sharpened peak begins to shift towards lower temperatures (AFM-dominant). Close to ≈ 1 T, the peak quickly broadens into a double-peak feature right before the entire feature is suppressed in the field-polarized state. Again, we see the dance between AFM and FM interactions indicative of the $\text{SmTi}_3(\text{Sb,Sn})_4$ family, and the much more intertwined nature of the A(FM) ground state.

Figure 5(g,h) summarize the field-dependent magnetization and field-dependent heat capacity results as field-temperature phase diagrams. The background color contour is produced through the second-derivative of the magnetization curves, while the discrete points are derived from the field-dependent heat capacity results. Note that the heat capacity points in Figure 5(h) are determined as the centroid of the heat capacity peaks shown in Figure 5(f).

Our results highlight how the intrinsic tunability inherited from the (Sb,Sn) solid-solution imparts a complex and nuanced degree of freedom to the $\text{SmTi}_3(\text{Sb,Sn})_4$ family of kagome metals. Not only does the (Sb,Sn) synergistic doping stabilize the crystal structure through controlling the electron filling and the relevance of bonding/antibonding states, but we also gain the ability to tune and control the interplay between the AFM and FM interactions intrinsic to the system. Particularly within the kagome metals, where the alignment of the Fermi level with critical features in the electronic band diagram is critical, the complex interplay between composition, temperature, and field in $\text{SmTi}_3(\text{Sb,Sn})_4$ offers a unique perspective on materials development. The strategy of utilizing synergistic dopants to develop more complex intermetallic materials is intriguing, as it is possible we are missing whole swaths intermetallic families without corresponding “pure” endpoints.

D. Brief Commentary on $\text{Ln}:(\text{Ce}, \text{Pr}, \text{Nd}, \text{Gd})$

For brevity and focus, this manuscript focused primarily on the properties of $\text{SmTi}_3(\text{Sb,Sn})_4$ series. For completeness we will briefly comment on the properties for the other rare-earth containing $\text{LnTi}_3(\text{Sb,Sn})_4$, with analogous characterization and details shown in the supplementary information.

NdTi₃(Sb,Sn)₄: The Nd-containing series shows properties remarkably similar to the $\text{SmTi}_3(\text{Sb,Sn})_4$ series. The Sn-rich terminus resembles a FM ground state with

onset of magnetic order around 10 K (see Supplemental Figure X) while Sb-rich $\text{NdTi}_3(\text{Sb,Sn})_4$ is very similar to the A(FM) state in Sb-rich $\text{SmTi}_3(\text{Sb,Sn})_4$, demonstrating field-induced metamagnetic transitions with appreciable coercivity. Note that the magnetic anisotropy has changed, however, as $\text{NdTi}_3(\text{Sb,Sn})_4$ compounds exhibit easy *b*-axis magnetization.

GdTi₃(Sb,Sn)₄: The Gd-containing series exhibits substantially less dependence on the (Sb,Sn) composition despite having a relatively wide solubility range. Both the Sb-rich and Sn-rich compositions show onset of antiferromagnetic order around 10-15 K and a clear metamagnetic transition when fields are directed along either *a* or *c*. The saturation moment is consistent with the full Gd^{3+} moment. These results suggest that this compound may have a non-collinear AFM structure or other complex anisotropy.

CeTi₃(Sb,Sn)₄: The Ce-containing compound exhibits an AFM cusp at 10 K followed by a FM-like (easy *b*-axis) response that saturates upon cooling below 3 K. Properties are broadly consistent with the magnetization behavior seen in the Sn-rich $\text{SmTi}_3(\text{Sb,Sn})_4$ series. Field-dependent measurements at 8 K confirm AFM (metamagnetic) nature of the 10 K peak.

PrTi₃(Sb,Sn)₄: The Pr-containing compound exhibits a broad magnetization rise below approximately 5.5 K. Perhaps $\text{PrTi}_3(\text{Sb,Sn})_4$ exhibits features similar to the rest of the rare-earth compounds (e.g. a broad AFM shoulder followed by a FM rise with easy *b*-axis magnetization), but the details are not clear. The case of Pr is further complicated by the known sensitivity of the Pr ion to local disorder and CEF effects.

While brief, we believe that this summary (alongside the characterization data in the supplementary) will be sufficient for others to peruse the critical features of the other $\text{LnTi}_3(\text{Sb,Sn})_4$ compounds and identify potential avenues for future research in those compounds.

IV. CONCLUSIONS

In this work we presented the single-crystal synthesis and characterization of the $\text{LnTi}_3(\text{Sb,Sn})_4$ series, a family which forms only as a solid-solution between the hypothetical LnTi_3Sn_4 and LnTi_3Sb_4 endpoints. We began our discussion by synthesizing the full range of $\text{LnTi}_3(\text{Sb,Sn})_4$ (*Ln*: Ce–Gd) single crystals. We demonstrate an extended solid-solution in $\text{NdTi}_3(\text{Sb,Sn})_4$, $\text{GdTi}_3(\text{Sb,Sn})_4$, and $\text{SmTi}_3(\text{Sb,Sn})_4$ along with controllable incorporation of (Sb,Sn) by tuning the composition of the flux. We hypothesized that the $\text{LnTi}_3(\text{Sb,Sn})_4$ series is electronically stabilized by the (Sb,Sn) alloying. We subsequently employed a combination of ARPES, DFT, and COHP measurements to show that the (Sb,Sn) pair tunes E_F without appreciably changing the bulk crystal structure (0.3% volumetric expansion) or the bulk electronic structure. Furthermore, (Sb,Sn) alloying appears to be strongly favored through (1) mini-

mization of the density-of-states at E_F , (2) population of unfilled bonding states when alloying Sb into hypothetical $LnTi_3Sn_4$, and (3) depopulation of filled antibonding states when alloying Sn into hypothetical $LnTi_3Sb_4$. These results culminate in the (Sb,Sn) pair serving not only as an effective means to tune E_F , but also a stabilizing force that stabilizes the $LnTi_3(Sb,Sn)_4$ crystal structure without deleterious effects on the electronic structure – an effect we have dubbed “synergistic doping.”

The (Sb,Sn) solid-solution also presents a unique opportunity to control the underlying electronic and magnetic properties of kagome metals, which is a persistent challenge in the development of new kagome metals. We chose to focus on the $SmTi_3(Sb,Sn)_4$ series for a detailed discussion of the (Sb,Sn) doping on the physical properties, demonstrating a complex, tunable interaction between competing AFM and FM ground states. In the Sn-rich sample, the AFM and FM transitions are separated by ≈ 10 K and the FM state competes with and eventually suppresses the AFM state. In the Sb-rich sample, however, the AFM and FM order appear to emerge nearly simultaneously into a state we called A(FM). At this point we cannot definitively determine the magnetic ground state of the Sb-rich composition, but it is very likely either an AFM structure with substantial spin canting, a ferrimagnet, or a candidate for a spin-density wave or other spin texture. While our discussion focused on the $SmTi_3(Sb,Sn)_4$ series, we briefly comment on the (Sb,Sn) alloying in the other rare-earth compounds (Ce, Pr, Nd, Gd) and provide additional details in supplementary information.

Ultimately this work accomplishes two goals: (1) to present a new family of cleavable, air-stable kagome metals with complex magnetic ground states and high potential for correlated phenomena, and (2) use the (Sb,Sn) alloying in $LnTi_3(Sb,Sn)_4$ to understand and propose a potentially new way of searching for complex intermetallics through the application of “synergistic doping.”

V. ACKNOWLEDGMENTS

Notice: This manuscript has been authored by UT-Battelle, LLC, under contract DE-AC05-00OR22725 with the US Department of Energy (DOE). The US government retains and the publisher, by accepting the article for publication, acknowledges that the US

government retains a nonexclusive, paid-up, irrevocable, worldwide license to publish or reproduce the published form of this manuscript, or allow others to do so, for US government purposes. DOE will provide public access to these results of federally sponsored research in accordance with the DOE Public Access Plan (<https://www.energy.gov/doe-public-access-plan>).

This work (sample discovery, single-crystal synthesis, bulk properties measurements, ARPES, manuscript authoring), was primarily supported by the U.S. Department of Energy (DOE), Office of Science, Basic Energy Sciences (BES), Materials Sciences and Engineering Division. M.N., M.S., and A.K.K. (ARPES) acknowledge support from the National Science Foundation, Division of Materials Research, under Award No. 2518800. G.D.S. (DFT) acknowledges support from the Laboratory Directed Research and Development Program of Oak Ridge National Laboratory, managed by UTBattelle, LLC, for the US Department of Energy. This research used resources of the Compute and Data Environment for Science (CADES) at the Oak Ridge National Laboratory, which is supported by the Office of Science of the U.S. Department of Energy under Contract No. DE-AC05-00OR22725. This research used resources of the Advanced Light Source, a U.S. Department of Energy Office of Science User Facility, under Contract No. DE-AC02-05CH11231. This research used resources at 21-ID-1 beamline of the National Synchrotron Light Source II, a US Department of Energy Office of Science User Facility operated for the DOE Office of Science by Brookhaven National Laboratory under contract no. DE-SC0012704. Preliminary single-crystal neutron diffraction measurements on TOPAZ at the Spallation Neutron Source, a U.S. Department of Energy Office of Science User Facility operated by Oak Ridge National Laboratory, were carried out under IPTS-35625.1.

VI. SUPPLEMENTARY INFO.

Supplementary ARPES data on the Sb-rich and Sn-rich endpoints; Supplementary ARPES data showing comparison with $SmTi_3Bi_4$; Full set of COHP simulations; full set of MvH, MvT, CvT curves for alloy series with quantitative axes; Supplementary characterization data for $NdTi_3(Sb,Sn)_4$, $GdTi_3(Sb,Sn)_4$, $CeTi_3(Sb,Sn)_4$, and $PrTi_3(Sb,Sn)_4$; Corresponding CIF files and crystallographic table for Sb-rich endpoints;

-
- [1] T. Park, M. Ye, and L. Balents, Electronic instabilities of kagome metals: saddle points and Landau theory, *Phys. Rev. B* **104**, 035142 (2021).
 [2] W.-S. Wang, Z.-Z. Li, Y.-Y. Xiang, and Q.-H. Wang, Competing electronic orders on kagome lattices at van hove filling, *Phys. Rev. B* **87**, 115135 (2013).

- [3] M. L. Kiesel, C. Platt, and R. Thomale, Unconventional Fermi surface instabilities in the kagome Hubbard model, *Phys. Rev. Lett.* **110**, 126405 (2013).
 [4] M. Jovanovic and L. M. Schoop, Simple chemical rules for predicting band structures of kagome materials, *Journal of the American Chemical Society* **144**, 10978 (2022).

- [5] B. R. Ortiz, L. C. Gomes, J. R. Morey, M. Winiarski, M. Bordelon, J. S. Mangum, I. W. Oswald, J. A. Rodriguez-Rivera, J. R. Neilson, S. D. Wilson, *et al.*, New kagome prototype materials: discovery of KV_3Sb_5 , RbV_3Sb_5 , and CsV_3Sb_5 , *Phys. Rev. Materials* **3**, 094407 (2019).
- [6] B. R. Ortiz, S. M. Teicher, Y. Hu, J. L. Zuo, P. M. Sarte, E. C. Schueller, A. M. Abeykoon, M. J. Krogstad, S. Rosenkranz, R. Osborn, R. Seshadri, L. Balents, J. He, and S. D. Wilson, CsV_3Sb_5 : a Z_2 topological kagome metal with a superconducting ground state, *Phys. Rev. Lett.* **125**, 247002 (2020).
- [7] S. D. Wilson and B. R. Ortiz, A v_3sb_5 kagome superconductors, *Nature Reviews Materials* **9**, 420 (2024).
- [8] Y. Wang, H. Wu, G. T. McCandless, J. Y. Chan, and M. N. Ali, Quantum states and intertwining phases in kagome materials, *Nature Reviews Physics* **5**, 635 (2023).
- [9] J.-X. Yin, B. Lian, and M. Z. Hasan, Topological kagome magnets and superconductors, *Nature* **612**, 647 (2022).
- [10] T. Neupert, M. M. Denner, J.-X. Yin, R. Thomale, and M. Z. Hasan, Charge order and superconductivity in kagome materials, *Nature Physics* **18**, 137 (2022).
- [11] D. Di Sante, T. Neupert, G. Sangiovanni, R. Thomale, R. Comin, J. G. Checkelsky, I. Zeljkovic, and S. D. Wilson, Kagome metals, *Reviews of Modern Physics* **98**, 015002 (2026).
- [12] K. Jiang, T. Wu, J.-X. Yin, Z. Wang, M. Z. Hasan, S. D. Wilson, X. Chen, and J. Hu, Kagome superconductors av_3sb_5 ($a = k, rb, cs$), *National Science Review* **10**, nwac199 (2023).
- [13] Q. Wang, H. Lei, Y. Qi, and C. Felser, Topological quantum materials with kagome lattice, *Accounts of Materials Research* **5**, 786 (2024).
- [14] Y. Liu, Z.-Y. Liu, J.-K. Bao, P.-T. Yang, L.-W. Ji, J.-Y. Liu, C.-C. Xu, W.-Z. Yang, W.-L. Chai, J.-Y. Lu, *et al.*, Superconductivity emerged from density-wave order in a kagome bad metal, **2023**, arXiv:2309.13514 [cond-mat.supr-con]. arXiv.org e-Print archive. //https://arxiv.org/pdf/2309.13514 (Accessed 6-25-2024).
- [15] D. Werhahn, B. R. Ortiz, A. K. Hay, S. D. Wilson, R. Seshadri, and D. Johrendt, The kagomé metals $RbTi_3Bi_5$ and $CsTi_3Bi_5$, *Z. Naturforsch. B* **77**, 757 (2022).
- [16] B. R. Ortiz, W. R. Meier, G. Pokharel, J. Chamorro, F. Yang, S. Mozaffari, A. Thaler, S. J. Gomez Alvarado, H. Zhang, D. S. Parker, *et al.*, Stability frontiers in the $am_6 \times 6$ kagome metals: The $ln_{nb_6sn_6}$ ($ln: Ce-lu, y$) family and density-wave transition in $ln_{nb_6sn_6}$, *Journal of the American Chemical Society* **147**, 5279 (2025).
- [17] H. W. S. Arachchige, W. R. Meier, M. Marshall, T. Matsuoka, R. Xue, M. A. McGuire, R. P. Hermann, H. Cao, and D. Mandrus, Charge density wave in kagome lattice intermetallic scv_6sn_6 , *Physical Review Letters* **129**, 216402 (2022).
- [18] X. Teng, L. Chen, F. Ye, E. Rosenberg, Z. Liu, J.-X. Yin, Y.-X. Jiang, J. S. Oh, M. Z. Hasan, K. J. Neubauer, *et al.*, Discovery of charge density wave in a kagome lattice antiferromagnet, *Nature* **609**, 490 (2022).
- [19] Y. Hu, J. Ma, Y. Li, Y. Jiang, D. J. Gawryluk, T. Hu, J. Teyssier, V. Multian, Z. Yin, S. Xu, S. Shin, I. Plokhikh, X. Han, N. C. Plumb, Y. Liu, J.-X. Yin, Z. Guguchia, Y. Zhao, A. P. Schnyder, X. Wu, E. Pomjakushina, M. Z. Hasan, N. Wang, and M. Shi, Phonon promoted charge density wave in topological kagome metal ScV_6Sn_6 , *Nature Communications* **15**, 1658 (2024).
- [20] W. R. Meier, R. P. Madhogaria, S. Mozaffari, M. Marshall, D. E. Graf, M. A. McGuire, H. W. S. Arachchige, C. L. Allen, J. Driver, H. Cao, *et al.*, Tiny sc allows the chains to rattle: impact of lu and y doping on the charge-density wave in scv_6sn_6 , *Journal of the American Chemical Society* **145**, 20943 (2023).
- [21] G. Pokharel, B. R. Ortiz, L. Kautzsch, S. J. Gomez Alvarado, K. Mallayya, G. Wu, E.-A. Kim, J. P. C. Ruff, S. Sarker, and S. D. Wilson, Frustrated charge order and cooperative distortions in ScV_6Sn_6 , *Physical Review Materials* **7**, 104201 (2023).
- [22] S. Cao, C. Xu, H. Fukui, T. Manjo, Y. Dong, M. Shi, Y. Liu, C. Cao, and Y. Song, Competing charge-density wave instabilities in the kagome metal ScV_6Sn_6 , *Nature Communications* **14**, 7671 (2023).
- [23] S. Lee, C. Won, J. Kim, J. Yoo, S. Park, J. Denlinger, C. Jozwiak, A. Bostwick, E. Rotenberg, R. Comin, M. Kang, and J.-H. Park, Nature of charge density wave in kagome metal scv_6sn_6 , *npj Quantum Materials* **9**, 15 (2024).
- [24] A. Korshunov, H. Hu, D. Subires, Y. Jiang, D. Călugăru, X. Feng, A. Rajapitamahuni, C. Yi, S. Roychowdhury, M. G. Vergniory, J. Stremper, C. Shekhar, E. Vescovo, D. Chernyshov, A. H. Said, A. Bosak, C. Felser, B. A. Bernevig, and S. Blanco-Canosa, Softening of a flat phonon mode in the kagome ScV_6Sn_6 , *Nature Communications* **14**, 6646 (2023).
- [25] H. Hu, Y. Jiang, D. Călugăru, X. Feng, D. Subires, M. G. Vergniory, C. Felser, S. Blanco-Canosa, and B. A. Bernevig, Kagome materials i: $Sg\ 191$, scv_6sn_6 . flat phonon soft modes and unconventional cdw formation: Microscopic and effective theory (2023).
- [26] S. Liu, C. Wang, S. Yao, Y. Jia, Z. Zhang, and J.-H. Cho, Driving mechanism and dynamic fluctuations of charge density waves in the kagome metal scv_6sn_6 , *Physical Review B* **109**, 1121103 (2024).
- [27] T. Yu, J. Lai, X. Liu, P. Liu, X.-Q. Chen, and Y. Sun, Magnetism and weak electronic correlations in the kagome metal ScV_6Sn_6 , *Physical Review B* **109**, 195145 (2024).
- [28] Y. Wang, Enhanced spin-polarization via partial g-dimerization as the driving force of the charge density wave in $fege$, *Physical Review Materials* **7**, 104006 (2023).
- [29] X. Wen, Y. Zhang, C. Li, Z. Gui, Y. Li, Y. Li, X. Wu, A. Wang, P. Yang, B. Wang, J. Cheng, Y. Wang, J. Ying, and X. Chen, Unconventional charge density wave in a kagome lattice antiferromagnet $fege$, *Physical Review Research* **6**, 033222 (2024).
- [30] Z. Chen, X. Wu, S. Zhou, J. Zhang, R. Yin, Y. Li, M. Li, J. Gong, M. He, Y. Chai, X. Zhou, Y. Wang, A. Wang, Y.-J. Yan, and D.-L. Feng, Discovery of a long-ranged charge order with $1/4$ ge_1 -dimerization in an antiferromagnetic kagome metal, *Nature Communications* **15**, 6262 (2024).
- [31] B. R. Ortiz, G. Pokharel, M. Gundayao, H. Li, F. Kaboudvand, L. Kautzsch, S. Sarker, J. P. Ruff, T. Hogan, S. J. G. Alvarado, *et al.*, YbV_3Sb_4 and EuV_3Sb_4 vanadium-based kagome metals with Yb^{2+} and Eu^{2+} zigzag chains, *Phys. Rev. Mater.* **7**, 064201 (2023).
- [32] B. R. Ortiz, H. Zhang, K. Górnicka, D. S. Parker, G. D. Samolyuk, F. Yang, H. Miao, Q. Lu, R. G. Moore, A. F. May, *et al.*, Intricate magnetic landscape in antiferromagnetic kagome metal tbt_3bi_4 and interplay with $ln_{2-x}ti_6+xbi_9$ ($ln: Tb \cdots lu$) shurikagome metals, *Chemistry of Materials* **36**, 8002 (2024).

- [33] B. R. Ortiz, H. Miao, D. S. Parker, F. Yang, G. D. Samolyuk, E. M. Clements, A. Rajapitamahuni, T. Yilmaz, E. Vescovo, J. Yan, *et al.*, Evolution of Highly Anisotropic Magnetism in the Titanium-Based Kagome Metals LnTi_3Bi_4 (Ln: La \cdots Gd $^{3+}$, Eu $^{2+}$, Yb $^{2+}$), *Chemistry of Materials* **35**, 9756 (2023).
- [34] A. Ovchinnikov and S. Bobev, Synthesis, Crystal and Electronic Structure of the Titanium Bismuthides $\text{Sr}_5\text{Ti}_{12}\text{Bi}_{19+x}$, $\text{Ba}_5\text{Ti}_{12}\text{Bi}_{19+x}$, and $\text{Sr}_{5-\delta}\text{Eu}_\delta\text{Ti}_{12}\text{Bi}_{19+x}$ ($x=0.5-1.0$; $\delta=2.4, 4.0$), *Eur. J. Inorg. Chem.* **2018**, 1266 (2018).
- [35] A. Ovchinnikov and S. Bobev, Bismuth as a reactive solvent in the synthesis of multicomponent transition-metal-bearing bismuthides, *Inorg. Chem.* **59**, 3459 (2019).
- [36] G. Motoyama, M. Sezaki, J. Gouchi, K. Miyoshi, S. Nishigori, T. Mutou, K. Fujiwara, and Y. Uwatoko, Magnetic properties of new antiferromagnetic heavy-fermion compounds, Ce_3TiBi_5 and CeTi_3Bi_4 , *Physica B Condens.* **536**, 142 (2018).
- [37] L. Chen, Y. Zhou, H. Zhang, X. Ji, K. Liao, Y. Ji, Y. Li, Z. Guo, X. Shen, R. Yu, *et al.*, Tunable magnetism in titanium-based kagome metals by rare-earth engineering and high pressure, *Communications Materials* **5**, 73 (2024).
- [38] J. Guo, L. Zhou, J. Ding, G. Qu, Z. Liu, Y. Du, H. Zhang, J. Li, Y. Zhang, F. Zhou, W. Qi, F. Guo, T. Wang, F. Fei, Y. Huang, T. Qian, D. Shen, H. Weng, and F. Song, Magnetic kagome materials RETi_3Bi_4 family with weak interlayer interactions, **2023**, arXiv:2308.14509v1 [cond-mat.mtrl-sci]. arXiv.org e-Print archive. <https://arxiv.org/pdf/2308.14509.pdf> (Accessed 10-24-2023).
- [39] E. Cheng, K. Wang, Y. Hao, W. Chen, H. Tan, Z. Li, M. Wang, W. Gao, D. Wu, S. Sun, *et al.*, Spectroscopic origin of giant anomalous hall effect in an interwoven magnetic kagome metal, arXiv preprint arXiv:2405.16831 (2024).
- [40] X. Han, H. Chen, Z. Cao, J. Guo, F. Fei, H. Tan, J. Guo, Y. Shi, R. Zhou, R. Wang, *et al.*, Discovery of unconventional charge-spin-intertwined density wave in magnetic kagome metal gdTi_3Bi_4 , arXiv preprint arXiv:2503.05545 (2025).
- [41] P. Park, B. R. Ortiz, M. Sprague, A. P. Sakhya, S. A. Chen, M. D. Frontzek, W. Tian, R. Sibille, D. G. Mazzone, C. Tabata, *et al.*, Spin density wave and van hove singularity in the kagome metal ceti_3Bi_4 , *Nature Communications* **16**, 4384 (2025).
- [42] M. I. Mondal, A. P. Sakhya, M. Sprague, B. R. Ortiz, M. Matzelle, A. K. Kumay, A. Seal, B. Ghosh, A. Bansil, and M. Neupane, Observation of multiple flat bands and van hove singularities in the distorted kagome metal ndTi_3Bi_4 , *Physical Review B* **112**, L121104 (2025).
- [43] Y. Hu, C. Le, L. Chen, H. Deng, Y. Zhou, N. C. Plumb, M. Radovic, R. Thomale, A. P. Schnyder, J.-X. Yin, *et al.*, Magnetic coupled electronic landscape in bilayer-distorted titanium-based kagome metals, *Physical Review B* **110**, L121114 (2024).
- [44] Z. Zheng, L. Chen, X. Ji, Y. Zhou, G. Qu, M. Hu, Y. Huang, H. Weng, T. Qian, and G. Wang, Anisotropic magnetism and band evolution induced by ferromagnetic phase transition in titanium-based kagome ferromagnet smti_3Bi_4 , *Science China Physics, Mechanics & Astronomy* **67**, 267411 (2024).
- [45] Z. Jiang, T. Li, J. Yuan, Z. Liu, Z. Cao, S. Cho, M. Shu, Y. Yang, Z. Li, J. Liu, *et al.*, Topological surface states in quasi-two-dimensional magnetic kagome metal eutl_3Bi_4 , *Science bulletin* **69**, 3192 (2024).
- [46] E. Cheng, N. Mao, X. Yang, B. Song, R. Lou, T. Ying, S. Nie, A. Fedorov, F. Bertran, P. Ding, *et al.*, Striped magnetization plateau and chirality-reversible anomalous hall effect in a magnetic kagome metal, arXiv preprint arXiv:2409.01365 (2024).
- [47] R. Zhang, B. Yu, H. Tan, Y. Cheng, A. Zong, Q. Hu, X. Chen, Y. Hu, C. Meng, J. Ren, *et al.*, Observation of orbital-selective band reconstruction in an anisotropic antiferromagnetic kagome metal tbt_3Bi_4 , arXiv preprint arXiv:2412.16815 (2024).
- [48] Y. Kushnirenko, L.-L. Wang, X. Su, A. Eaton, P. Canfield, A. Kaminski, B. Schruck, and E. O'Leary, Observation of band splitting and magnetically induced band structure reconstruction in tbt_3Bi_4 , *Physical Review B* **112**, 155119 (2025).
- [49] A. P. Sakhya, B. R. Ortiz, B. Ghosh, M. Sprague, M. I. Mondal, M. Matzelle, I. Bin Elius, N. Valadez, D. G. Mandrus, A. Bansil, *et al.*, Diverse electronic landscape of the kagome metal ybTi_3Bi_4 , *Communications Materials* **5**, 241 (2024).
- [50] A. P. Sakhya, B. R. Ortiz, B. Ghosh, M. Sprague, M. I. Mondal, M. Matzelle, N. Atlam, A. K. Kumay, D. G. Mandrus, J. D. Denlinger, *et al.*, Diverse electronic topography in a distorted kagome metal lati_3Bi_4 , arXiv preprint arXiv:2503.15759 (2025).
- [51] R. Zhang, B. Yu, H. Tan, Y. Cheng, F. Shen, J. Yang, D. Mu, X. Han, A. Zong, Q. Hu, *et al.*, Observation of orbital-selective dual modulations in an anisotropic antiferromagnetic kagome metal tbt_3Bi_4 , *Physical Review X* **15**, 031012 (2025).
- [52] J. Guo, S. Zhu, R. Zhou, R. Wang, Y. Wang, J. Sun, Z. Zhao, X. Dong, J. Cheng, H. Yang, *et al.*, Tunable bifurcation of magnetic anisotropy and bi-oriented antiferromagnetic order in kagome metal gdTi_3Bi_4 , *Physical Review Letters* **134**, 226704 (2025).
- [53] K. Shtefiienko, C. Phillips, B. R. Ortiz, D. E. Graf, and K. Shrestha, Electronic structure of the kagome metal ybTi_3Bi_4 studied using torque magnetometry, *Physical Review B* **111**, 035145 (2025).
- [54] X. Li, Y. Yang, F. Guan, X. Zhu, W. Ning, and M. Tian, Anisotropic magnetoresistance in antiferromagnetic kagome metal gdTi_3Bi_4 , *Applied Physics Letters* **126** (2025).
- [55] Y. Shu, X. Mi, Y. Wei, S. Tao, A. Wang, Y. Chai, D. Ma, X. Yang, and M. He, Complex magnetotransport in the paramagnetic state of the magnetic kagome metal eutl_3Bi_4 , *Physical Review B* **111**, 155103 (2025).
- [56] P. C. Canfield, T. Kong, U. S. Kaluarachchi, and N. H. Jo, Use of frit-disc crucibles for routine and exploratory solution growth of single crystalline samples, *Philosophical magazine* **96**, 84 (2016).
- [57] L. Coates, H. Cao, B. C. Chakoumakos, M. D. Frontzek, C. Hoffmann, A. Y. Kovalevsky, Y. Liu, F. Meilleur, A. M. dos Santos, D. A. Myles, *et al.*, A suite-level review of the neutron single-crystal diffraction instruments at oak ridge national laboratory, *Review of Scientific Instruments* **89** (2018).
- [58] W. Kohn and L. J. Sham, Self-consistent equations including exchange and correlation effects, *Physical review* **140**, A1133 (1965).

- [59] J. P. Perdew, K. Burke, and M. Ernzerhof, Generalized gradient approximation made simple, *Phys. Rev. Lett.* **77**, 3865 (1996).
- [60] P. E. Blöchl, Projector augmented-wave method, *Phys. Rev. B* **50**, 17953 (1994).
- [61] G. Kresse and J. Furthmüller, Efficiency of ab-initio total energy calculations for metals and semiconductors using a plane-wave basis set, *Comput. Mater. Sci.* **6**, 15 (1996).
- [62] G. Kresse and D. Joubert, From ultrasoft pseudopotentials to the projector augmented-wave method, *Phys. Rev. B* **59**, 1758 (1999).
- [63] V. L. Deringer, A. L. Tchougréeff, and R. Dronskowski, Crystal orbital hamilton population (cohp) analysis as projected from plane-wave basis sets, *The journal of physical chemistry A* **115**, 5461 (2011).
- [64] R. Dronskowski and P. E. Bloechl, Crystal orbital hamilton populations (cohp): energy-resolved visualization of chemical bonding in solids based on density-functional calculations, *The Journal of Physical Chemistry* **97**, 8617 (1993).
- [65] S. Maintz, V. L. Deringer, A. L. Tchougréeff, and R. Dronskowski, Analytic projection from plane-wave and paw wavefunctions and application to chemical-bonding analysis in solids, *Journal of computational chemistry* **34**, 2557 (2013).
- [66] S. Maintz, V. L. Deringer, A. L. Tchougréeff, and R. Dronskowski, Lobster: a tool to extract chemical bonding from plane-wave based dft (2016).
- [67] Y. Wang, P. C. Müller, D. Hemker, and R. Dronskowski, Loposter: a cascading postprocessor for lobster, *Journal of Computational Chemistry* **46**, e70167 (2025).
- [68] H. Bie, S. D. Moore, D. G. Piercey, A. V. Tkachuk, O. Y. Zelinska, and A. Mar, Ternary rare-earth titanium antimonides: phase equilibria in the RE–Ti–Sb (RE= La, Er) systems and crystal structures of $\text{RE}_2\text{Ti}_7\text{Sb}_{12}$ (RE= La, Ce, Pr, Nd) and $\text{RETi}_3(\text{Sn}_x\text{Sb}_{1-x})_4$ (RE= Nd, Sm), *J. Solid State Chem.* **180**, 2216 (2007).
- [69] B. R. Ortiz, H. Zhang, K. Górnicka, M. S. Cook, S. Sarker, S. Okamoto, and J. Yan, Isolated spin ladders in $\text{In}_2\text{Ti}_9\text{Sb}_{11}$ (In: La–Nd) metals, *Physical Review Materials* **9**, 086203 (2025).

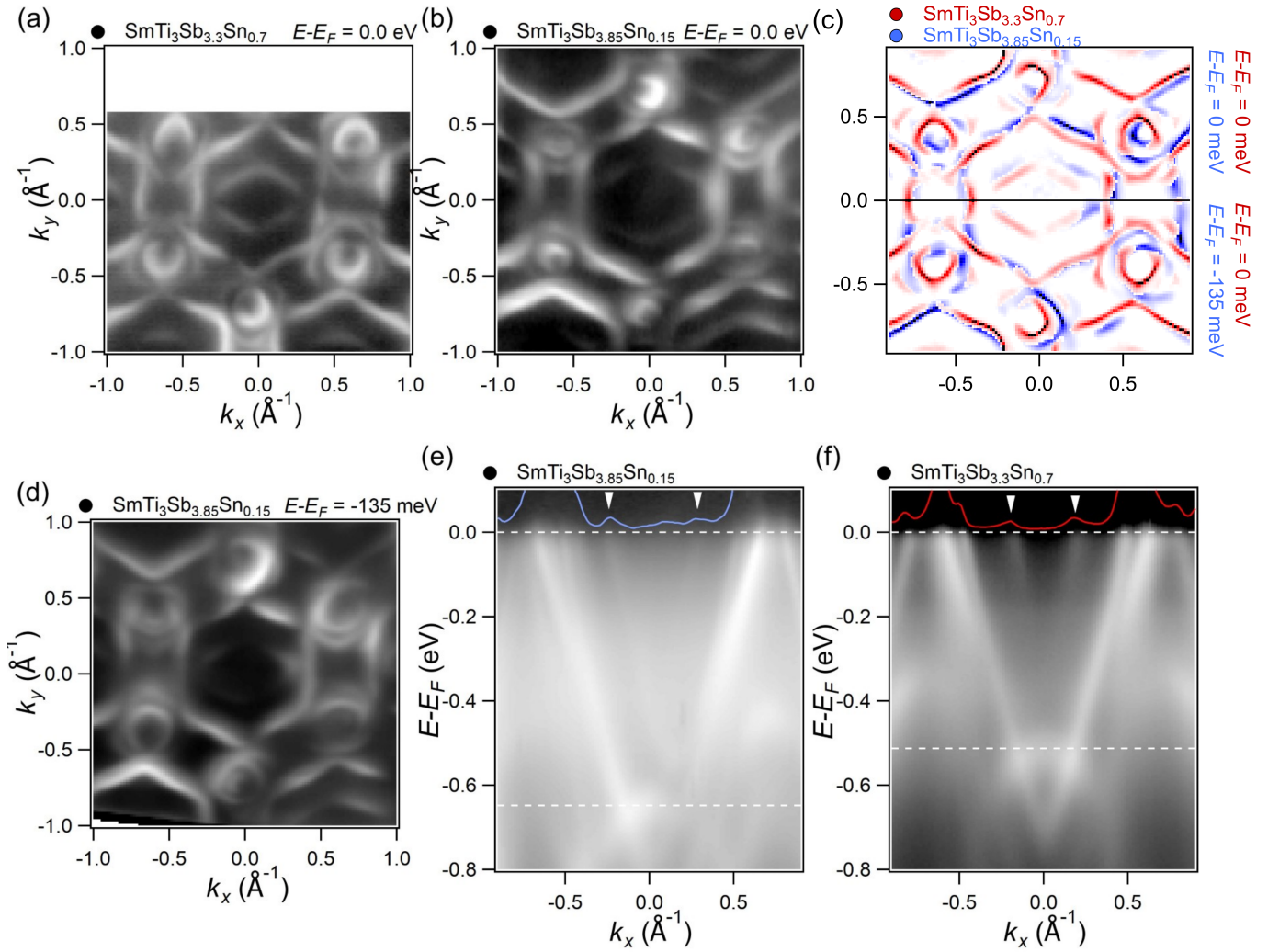


FIG. S1. Supplementary ARPES data collected on the Sn-Rich and Sb-Rich $\text{SmTi}_3(\text{Sb,Sn})_4$ series. (a) Constant energy contour (CEC) for Sb-rich $\text{SmTi}_3(\text{Sb,Sn})_4$ at the natural Fermi level. (b) CEC for Sn-rich $\text{SmTi}_3(\text{Sb,Sn})_4$ at the natural Fermi level. While the Sb-rich and Sn-rich compounds look broadly similar, there is a clear shift in the bands near Γ . (c) Comparison between the Sn-rich and Sb-rich ARPES scans at the natural Fermi level (top) and the same materials but with the Sb-rich CEC shifted to the -135 meV level. We can see that the bands near Γ are much more aligned with the 135 meV shift. This shift corresponds to the doping difference between the Sb-rich and Sn-rich $\text{SmTi}_3(\text{Sb,Sn})_4$. (d) CEC of the Sb-rich compound at the -135 meV Fermi level. (e,f) Same ARPES data shown in the main body, highlighting the bands near Γ and the Fermi level shift induced by the Sb-Sn doping.

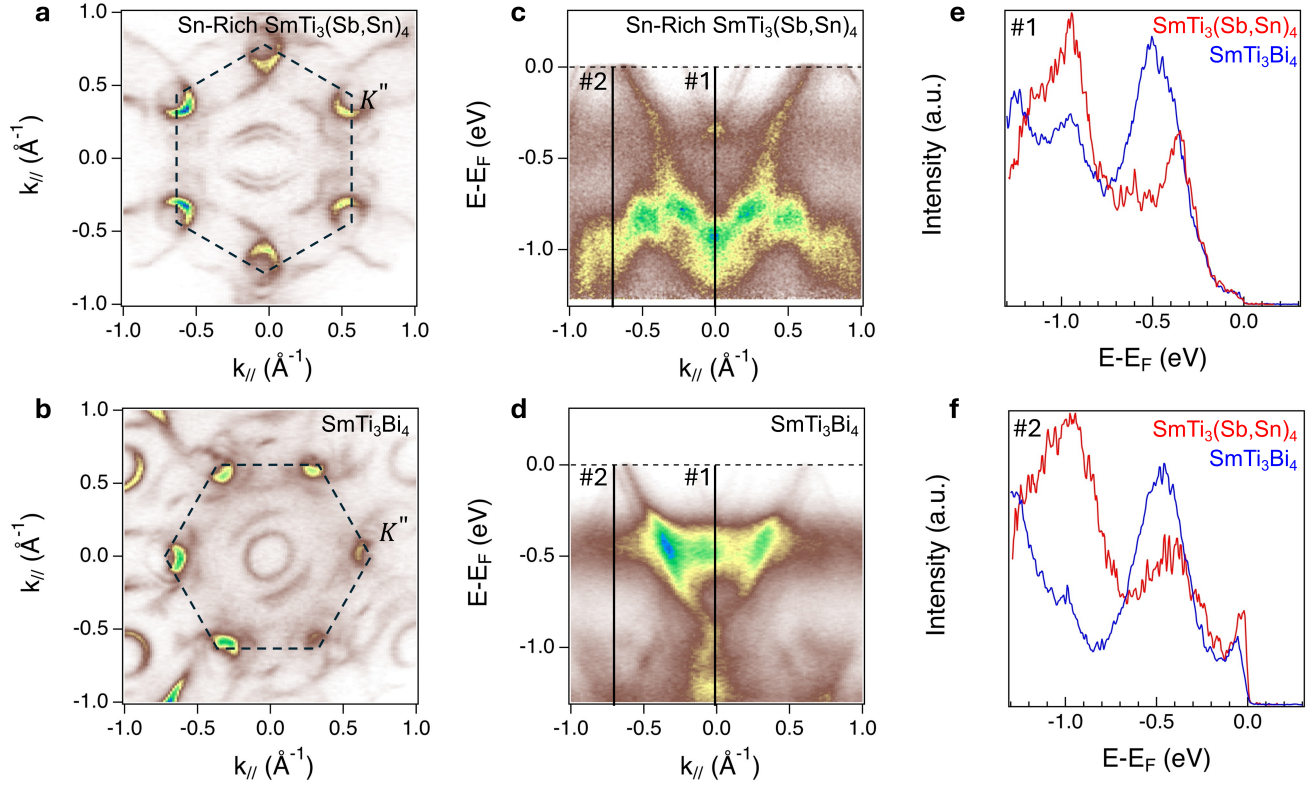


FIG. S2. Supplementary ARPES data collected on the Sb-rich $\text{SmTi}_3(\text{Sb,Sn})_4$ and the bismuthide SmTi_3Bi_4 . (a,b) Constant energy contour (CEC) ARPES data for $\text{SmTi}_3(\text{Sb,Sn})_4$ and SmTi_3Bi_4 , respectively. Dashed hexagons highlight the Brillouin zone boundary on the surface. (c,d) ARPES intensity plots along K-G-K direction, corresponding to the red dashed line shown in CEC plots. (e) Comparison of the energy distribution curves (EDCs) at the G point (cut 1). Blue and red EDC's represent SmTi_3Bi_4 and $\text{SmTi}_3(\text{Sb,Sn})_4$, respectively. (f) Comparison of EDC's at the K point (cut 2). Comparing with SmTi_3Bi_4 , the shift in the electronic structure of $\text{SmTi}_3(\text{Sb,Sn})_4$ is consistent with hole doping in $\text{SmTi}_3(\text{Sb,Sn})_4$.

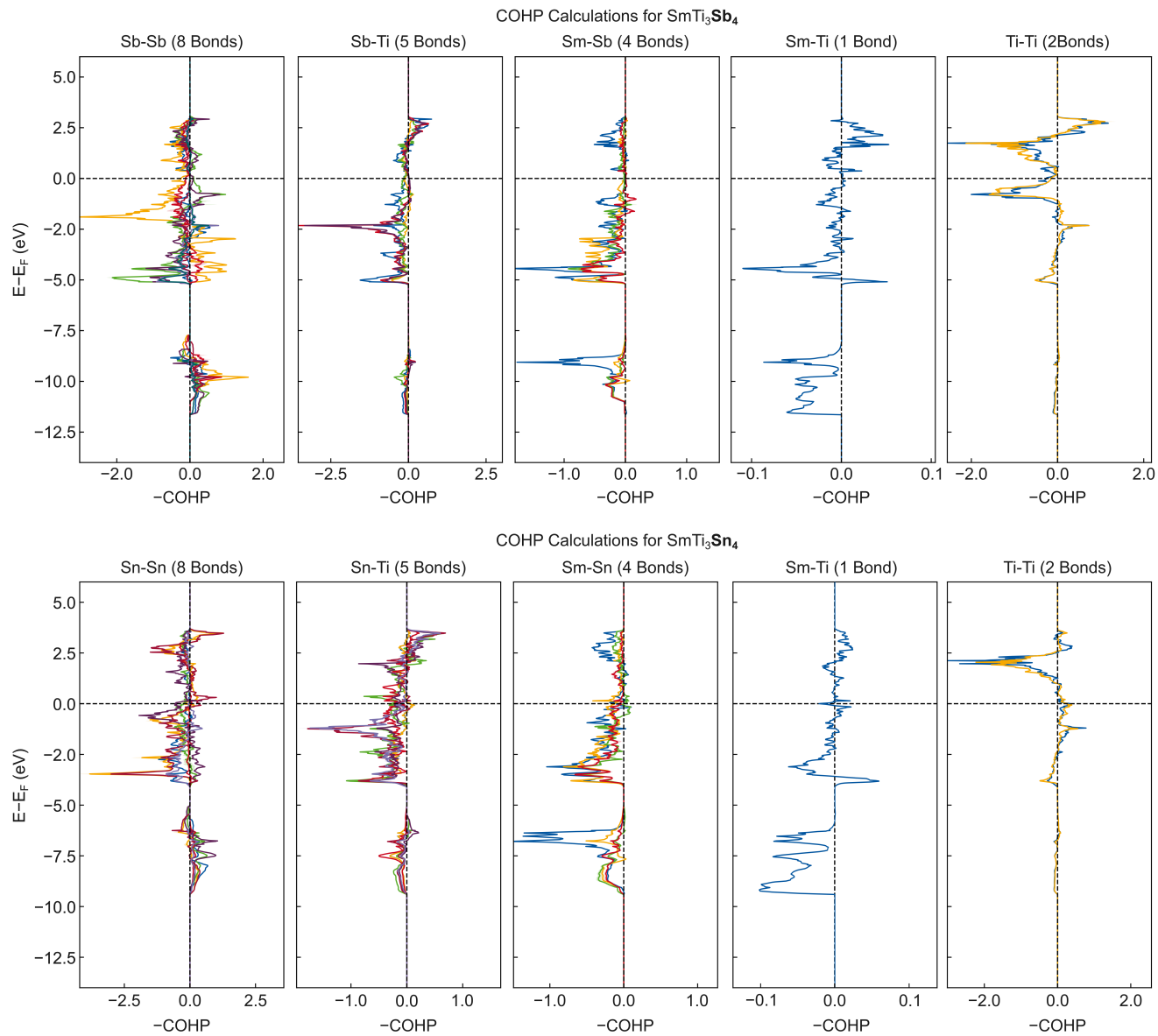


FIG. S3. Supplementary Crystal Orbital Hamilton Population (COHP) data for both SmTi_3Sb_4 (top 5 panels) and SmTi_3Sn_4 (bottom 5 panels). In the main body we focused on the Ti-Ti, Sb-Sb, and Sn-Sn interactions, but here we show all 5 types of interactions.

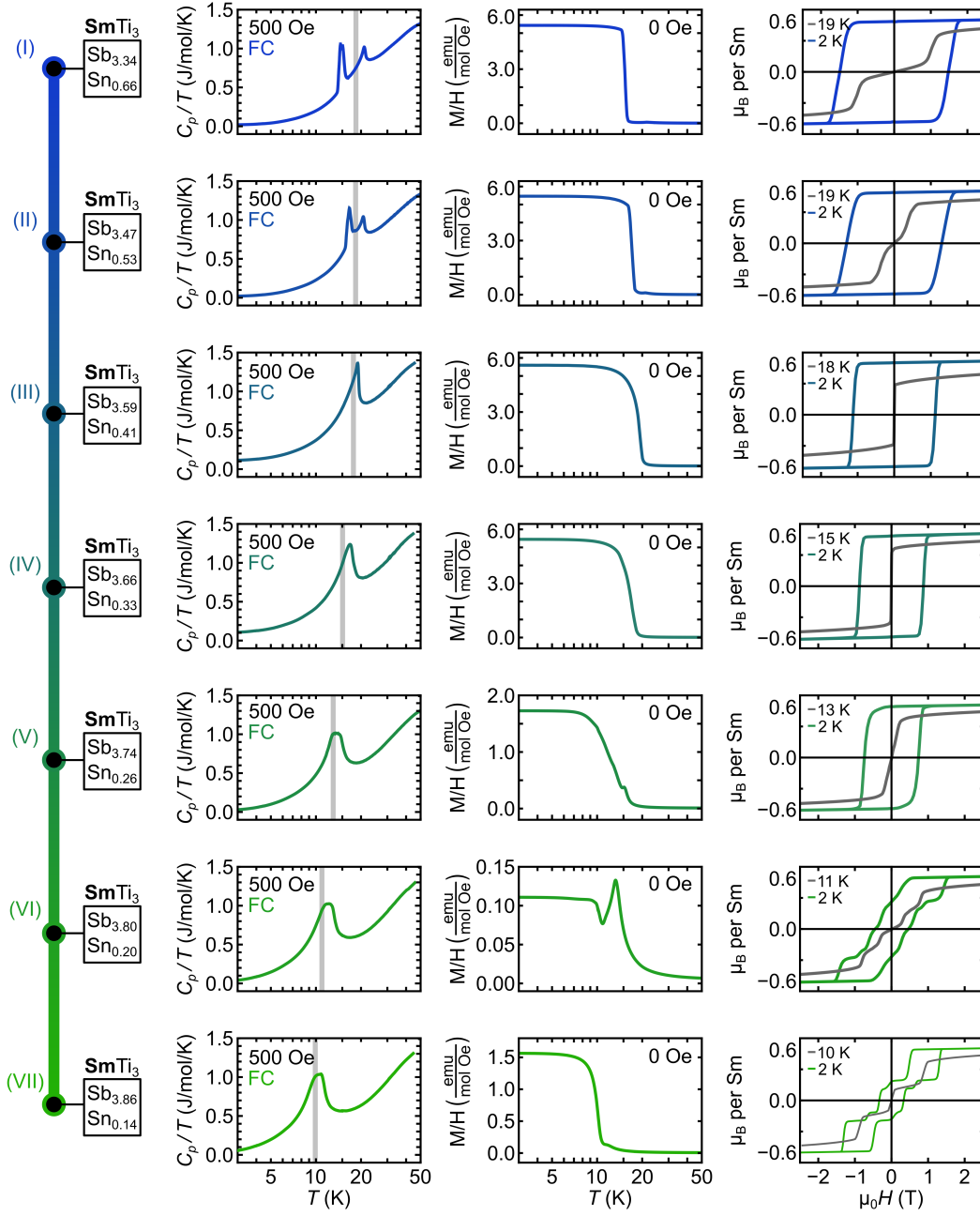


FIG. S4. Supplementary characterization data for the full series of samples traversing the $\text{SmTi}_3(\text{Sb,Sn})_4$ solid-solution to demonstrate the gradual shift in magnetic and thermodynamic properties. This is identical data to that shown in the main body, but separated onto individual axes for quantitative comparison. Shown from left to right are: (1) the measured (Sb,Sn) content of the single crystals, (2) a plot showing the temperature-dependent magnetization (3) zero-field heat capacity results, and (4) the corresponding isothermal magnetization curves at base temperature and an intermediate temperature (gray) intended to demarcate the transition between the two heat capacity features (where possible). For clarity, the intermediate temperature (gray) is also marked on the temperature-dependent magnetization.

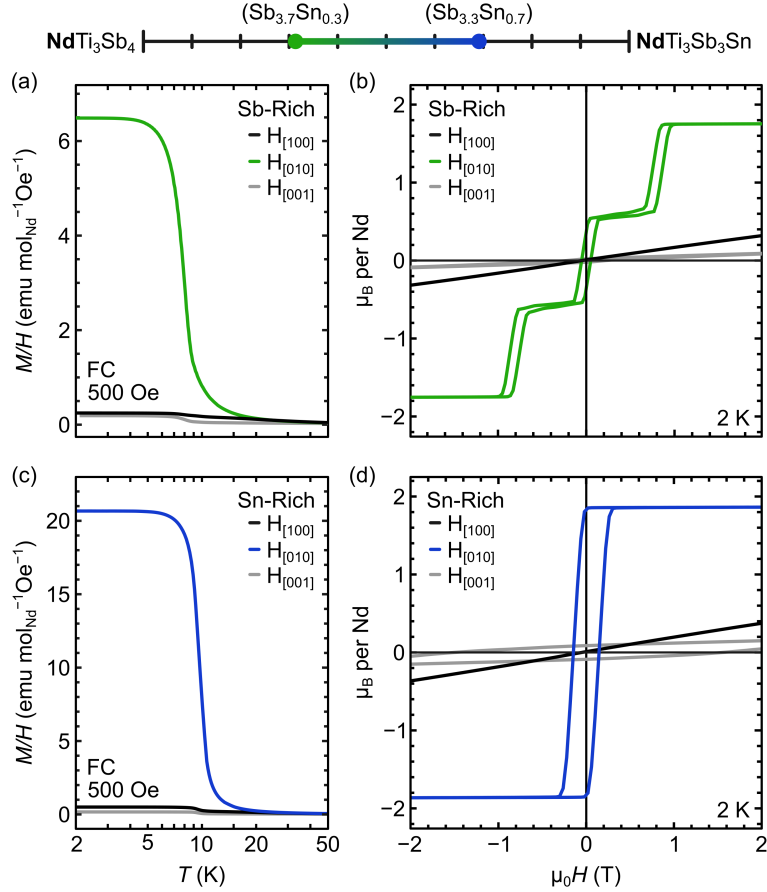


FIG. S5. Supplementary characterization data for $\text{NdTi}_3(\text{Sb,Sn})_4$ alloy series. The Nd-containing series shows properties remarkably reminiscent of the $\text{SmTi}_3(\text{Sb,Sn})_4$ data shown previously. Temperature-dependent magnetization for Sb-rich $\text{NdTi}_3(\text{Sb,Sn})_4$ (a) shows a broad peak with with a plateau which is weaker than would be expected for a prototypical FM. Isothermal magnetization results (b) reveal field-induced metamagnetic transitions with small but appreciable hysteresis in both transitions, reminiscent of the A(FM) state proposed for Sb-rich $\text{SmTi}_3(\text{Sb,Sn})_4$. Sn-rich $\text{NdTi}_3(\text{Sb,Sn})_4$ resembles a more prototypical FM with onset of magnetic order around 10 K in temperature-dependent magnetization measurements (c). Isothermal magnetization (d) confirms a FM response with a relatively weak coercive field less than 0.2 T. Note that $\text{NdTi}_3(\text{Sb,Sn})_4$ exhibits a easy-axis along *b*.

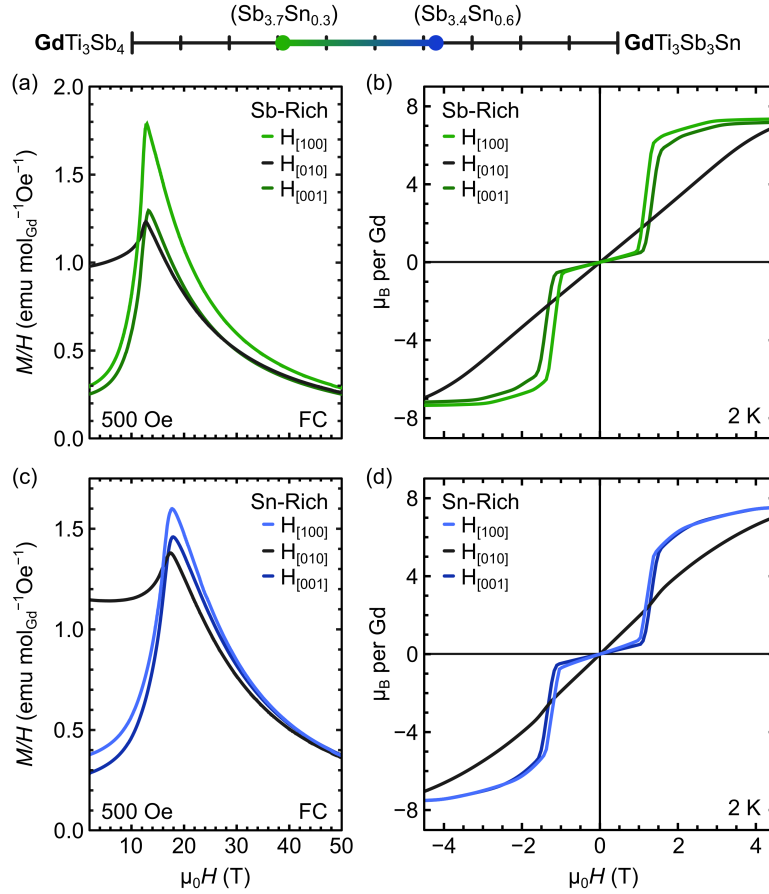


FIG. S6. Supplementary characterization data for $\text{GdTi}_3(\text{Sb,Sn})_4$ alloy series. The Gd-containing series shows properties consistent with the bismuthide GdTi_3Bi_4 published previously. Despite the substantial (Sb,Sn) solubility range in $\text{GdTi}_3(\text{Sb,Sn})_4$, the system is substantially less responsive to the doping, potentially due to the large spin-only moment of Gd^{3+} . Both the Sb-rich (a) and Sn-rich (c) temperature-dependent magnetization exhibit onset of AFM order around 13 K and 18 K, respectively. Both isothermal magnetization curves (b,d) are remarkably similar and plateau to values expected for the full Gd^{3+} moment. A clear field-induced spin-flop transition replete with a gradual spin reorientation is observed. Field-induced metamagnetism in the $\text{GdTi}_3(\text{Sb,Sn})_4$ series occurs for fields directed along either c or a , consistent with GdTi_3Bi_4 . These results suggest that this compound may have a non-collinear AFM structure or other complex anisotropy.

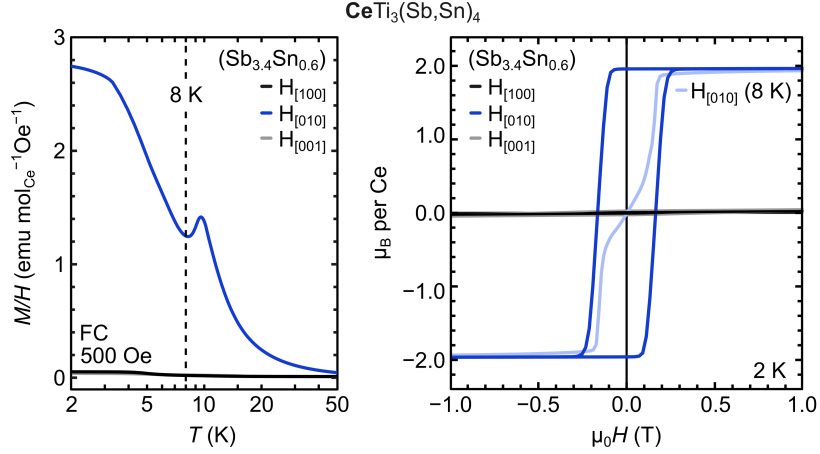


FIG. S7. Supplementary characterization data for CeTi₃(Sb,Sn)₄ alloy series. The Ce-containing compound exhibits an AFM cusp at 10 K followed by a FM-like (easy b -axis) response that saturates upon cooling below 3 K. Properties are broadly consistent with the magnetization behavior seen in the Sn-rich SmTi₃(Sb,Sn)₄ series. Field-dependent measurements at 8 K confirm AFM (metamagnetic) nature of the 10 K peak. As in Sn-rich SmTi₃(Sb,Sn)₄, the AFM response appears to be suppressed and replaced with FM order by 2 K.

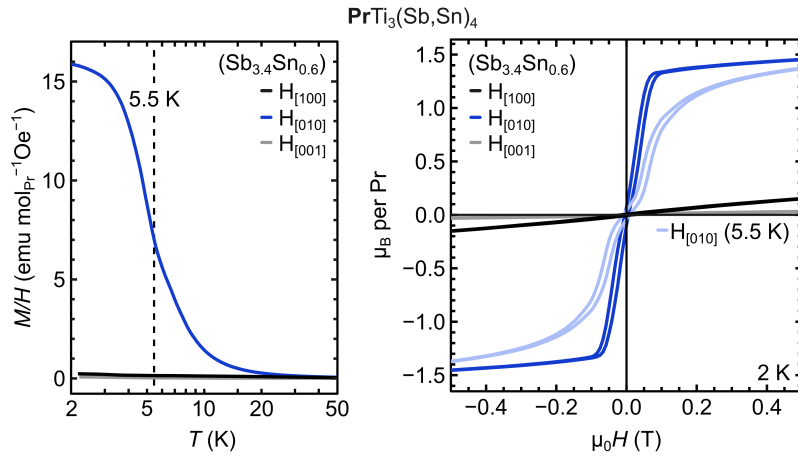


FIG. S8. Supplementary characterization data for PrTi₃(Sb,Sn)₄ alloy series. The Pr-containing compound exhibits a broad magnetization rise below approximately 5.5 K. Perhaps PrTi₃(Sb,Sn)₄ exhibits features similar to the rest of the rare-earth compounds (e.g. a broad AFM shoulder followed by a FM rise with easy b -axis magnetization), but the details are not clear. The case of Pr is further complicated by the known sensitivity of the Pr-ion to local disorder and CEF effects.

TABLE I. Abbreviated summary of supplementary crystal data, structural refinement, and atomic positions for Sb-rich $\text{SmTi}_3(\text{Sb},\text{Sn})_4$. Specific composition is $\text{SmTi}_3\text{Sb}_{3.86}\text{Sn}_{0.14}$ (corresponding to green data traces in main body). Complete CIF file is provided in the supplementary information. Specific (Sb,Sn) composition is set by spectroscopic methods and is assumed to be distributed randomly across all Sb sites based on preliminary neutron diffraction data.

Crystal Data and Refinement		Atomic Positions (fractional coordinates)					
Property	Value	Label	x	y	z	U_{iso}	Occ.
Formula	$\text{SmTi}_3\text{Sb}_{3.86}\text{Sn}_{0.14}$	Sm01	1	1/2	0.69540(2)	0.00767(10)	1
Space group, Z	Fmmm, 8	Ti01	1/2	1/2	0.59181(5)	0.0071(2)	1
a (Å)	5.76500(10)	Ti02	1/4	1/4	0.40441(3)	0.00664(15)	1
b (Å)	10.0901(2)	Sb01	1/2	0.32901(4)	1/2	0.00753(11)	0.9647
c (Å)	24.0655(5)	Sn01	"	"	"	"	0.0353
Volume (Å ³)	1399.88(5)	Sb02	0	0.15948(3)	0.31149(2)	0.00736(9)	0.9647
Density (calc.) (g cm ⁻³)	7.408	Sn02	"	"	"	"	0.0353
R_{int} , Completeness	0.0230, 99%	Sb03	1	1/2	0.56641(2)	0.00731(11)	0.9647
R_1 [$I > 2\sigma(I)$]	0.0226	Sn03	"	"	"	"	0.0353
wR_2 [$I > 2\sigma(I)$]	0.0677						
Largest peak/hole (e Å ⁻³)	3.291 / -2.737						

TABLE II. Abbreviated summary of supplementary crystal data, structural refinement, and atomic positions for Sn-rich $\text{SmTi}_3(\text{Sb},\text{Sn})_4$. Specific composition is $\text{SmTi}_3\text{Sb}_{3.338}\text{Sn}_{0.662}$ (corresponding to blue data traces in main body). Complete CIF file is provided in the supplementary information. Specific (Sb,Sn) composition is set by spectroscopic methods and is assumed to be distributed randomly across all Sb sites based on preliminary neutron diffraction data.

Crystal Data and Refinement		Atomic Positions (fractional coordinates)					
Property	Value	Label	x	y	z	U_{iso}	Occ.
Formula	$\text{SmTi}_3\text{Sb}_{3.338}\text{Sn}_{0.662}$	Sm01	1	1/2	0.69508(2)	0.0075(2)	1
Space group, Z	Fmmm, 8	Ti01	1/2	1/2	0.59269(9)	0.0077(4)	1
a (Å)	5.7582(3)	Ti02	1/4	1/4	0.40362(6)	0.0068(3)	1
b (Å)	10.0696(5)	Sb01	1/2	0.32890(8)	1/2	0.0088(2)	0.8345
c (Å)	24.1350(11)	Sn01	"	"	"	"	0.1655
Volume (Å ³)	1399.41(12)	Sb02	0	0.16014(5)	0.31100(2)	0.0073(2)	0.8345
Density (calc.) (g cm ⁻³)	7.395	Sn02	"	"	"	"	0.1655
R_{int} , Completeness	0.0344, 98.3%	Sb03	1	1/2	0.56622(3)	0.0077(2)	0.8345
R_1 [$I > 2\sigma(I)$]	0.0335	Sn03	"	"	"	"	0.1655
wR_2 [$I > 2\sigma(I)$]	0.0838						
Largest peak/hole (e Å ⁻³)	3.703 / -2.649						

TABLE III. Abbreviated summary of supplementary crystal data, structural refinement, and atomic positions for Sb-rich $\text{CeTi}_3(\text{Sb},\text{Sn})_4$. Specific composition is $\text{CeTi}_3\text{Sb}_{3.38}\text{Sn}_{0.62}$ (corresponding to green data traces in main body). Complete CIF file is provided in the supplementary information. Specific (Sb,Sn) composition is set by spectroscopic methods and is assumed to be distributed randomly across all Sb sites based on preliminary neutron diffraction data.

Crystal Data and Refinement		Atomic Positions (fractional coordinates)					
Property	Value	Label	x	y	z	U_{iso}	Occ.
Formula	CeTi₃Sb_{3.38}Sn_{0.62}	Ce01	1	1/2	0.69513(4)	0.0099(2)	1
Space group, Z	Fmmm, 8	Ti01	1/2	1/2	0.59171(15)	0.0103(6)	1
a (Å)	5.8102(8)	Ti02	1/4	1/4	0.40523(9)	0.0086(4)	1
b (Å)	10.1127(13)	Sb01	1/2	0.32947(14)	1/2	0.0120(3)	0.845
c (Å)	24.402(3)	Sn01	"	"	"	"	0.155
Volume (Å ³)	1433.8(3)	Sb02	0	0.16112(9)	0.31356(4)	0.0097(2)	0.845
Density (calc.) (g cm ⁻³)	7.124	Sn02	"	"	"	"	0.155
R_{int} , Completeness	0.0888, 99.3%	Sb03	1	1/2	0.56523(5)	0.0103(3)	0.8455
R_1 [$I > 2\sigma(I)$]	0.0543	Sn03	"	"	"	"	0.155
wR_2 [$I > 2\sigma(I)$]	0.1143						
Largest peak/hole (e Å ⁻³)	4.526 / -3.423						

TABLE IV. Abbreviated summary of supplementary crystal data, structural refinement, and atomic positions for Sb-rich $\text{PrTi}_3(\text{Sb},\text{Sn})_4$. Specific composition is $\text{PrTi}_3\text{Sb}_{3.365}\text{Sn}_{0.635}$ (corresponding to green data traces in main body). Complete CIF file is provided in the supplementary information. Specific (Sb,Sn) composition is set by spectroscopic methods and is assumed to be distributed randomly across all Sb sites based on preliminary neutron diffraction data.

Crystal Data and Refinement		Atomic Positions (fractional coordinates)					
Property	Value	Label	x	y	z	U_{iso}	Occ.
Formula	PrTi₃Sb_{3.365}Sn_{0.635}	Pr01	1	1/2	0.69503(2)	0.00792(10)	1
Space group, Z	Fmmm, 8	Ti01	1/2	1/2	0.59221(6)	0.0080(2)	1
a (Å)	5.7999(2)	Ti02	1/4	1/4	0.40457(4)	0.00728(16)	1
b (Å)	10.1034(4)	Sb01	1/2	0.32929(5)	1/2	0.00967(11)	0.8412
c (Å)	24.3298(9)	Sn01	"	"	"	"	0.1588
Volume (Å ³)	1425.69(9)	Sb02	0	0.16096(4)	0.31269(2)	0.00796(9)	0.8412
Density (calc.) (g cm ⁻³)	7.172	Sn02	"	"	"	"	0.1587
R_{int} , Completeness	0.0302, 99.8%	Sb03	1	1/2	0.56531(2)	0.00842(11)	0.8412
R_1 [$I > 2\sigma(I)$]	0.0286	Sn03	"	"	"	"	0.1588
wR_2 [$I > 2\sigma(I)$]	0.0666						
Largest peak/hole (e Å ⁻³)	3.024 / -1.751						

TABLE V. Abbreviated summary of supplementary crystal data, structural refinement, and atomic positions for Sb-rich $\text{NdTi}_3(\text{Sb},\text{Sn})_4$. Specific composition is $\text{NdTi}_3\text{Sb}_{3.29}\text{Sn}_{0.71}$ (corresponding to green data traces in main body). Complete CIF file is provided in the supplementary information. Specific (Sb,Sn) composition is set by spectroscopic methods and is assumed to be distributed randomly across all Sb sites based on preliminary neutron diffraction data.

Crystal Data and Refinement		Atomic Positions (fractional coordinates)					
Property	Value	Label	x	y	z	U_{iso}	Occ.
Formula	$\text{NdTi}_3\text{Sb}_{3.29}\text{Sn}_{0.71}$	Nd01	1	1/2	0.69504(2)	0.00780(9)	1
Space group, Z	Fmmm, 8	Ti01	1/2	1/2	0.59238(5)	0.0076(2)	1
a (Å)	5.7839(3)	Ti02	1/4	1/4	0.40421(3)	0.00694(14)	1
b (Å)	10.0918(5)	Sb01	1/2	0.32910(5)	1/2	0.00923(10)	0.8225
c (Å)	24.2738(13)	Sn01	"	"	"	"	0.1775
Volume (Å ³)	1416.86(13)	Sb02	0	0.16062(3)	0.31207(2)	0.00762(9)	0.8225
Density (calc.) (g cm ⁻³)	7.245	Sn02	"	"	"	"	0.1775
R_{int} , Completeness	0.0263, 99.1%	Sb03	1	1/2	0.56559(2)	0.00793(10)	0.8225
R_1 [$I > 2\sigma(I)$]	0.0257	Sn03	"	"	"	"	0.1775
wR_2 [$I > 2\sigma(I)$]	0.0608						
Largest peak/hole (e Å ⁻³)	1.747 / -2.495						

TABLE VI. Abbreviated summary of supplementary crystal data, structural refinement, and atomic positions for Sb-rich $\text{GdTi}_3(\text{Sb},\text{Sn})_4$. Specific composition is $\text{GdTi}_3\text{Sb}_{3.373}\text{Sn}_{0.627}$ (corresponding to green data traces in main body). Complete CIF file is provided in the supplementary information. Specific (Sb,Sn) composition is set by spectroscopic methods and is assumed to be distributed randomly across all Sb sites based on preliminary neutron diffraction data.

Crystal Data and Refinement		Atomic Positions (fractional coordinates)					
Property	Value	Label	x	y	z	U_{iso}	Occ.
Formula	$\text{GdTi}_3\text{Sb}_{3.373}\text{Sn}_{0.627}$	Gd01	1	1/2	0.69527(2)	0.00765(9)	1
Space group, Z	Fmmm, 8	Ti01	1/2	1/2	0.59274(5)	0.0066(2)	1
a (Å)	5.7467(3)	Ti02	1/4	1/4	0.40345(4)	0.00650(16)	1
b (Å)	10.0645(6)	Sb01	1/2	0.32888(5)	1/2	0.00840(11)	0.8432
c (Å)	24.0610(14)	Sn01	"	"	"	"	0.1568
Volume (Å ³)	1391.63(14)	Sb02	0	0.15952(3)	0.31043(2)	0.00728(9)	0.8433
Density (calc.) (g cm ⁻³)	7.503	Sn02	"	"	"	"	0.1567
R_{int} , Completeness	0.0286, 99.8%	Sb03	1	1/2	0.56680(2)	0.00729(11)	0.8432
R_1 [$I > 2\sigma(I)$]	0.0270	Sn03	"	"	"	"	0.1568
wR_2 [$I > 2\sigma(I)$]	0.0662						
Largest peak/hole (e Å ⁻³)	2.545 / -3.031						

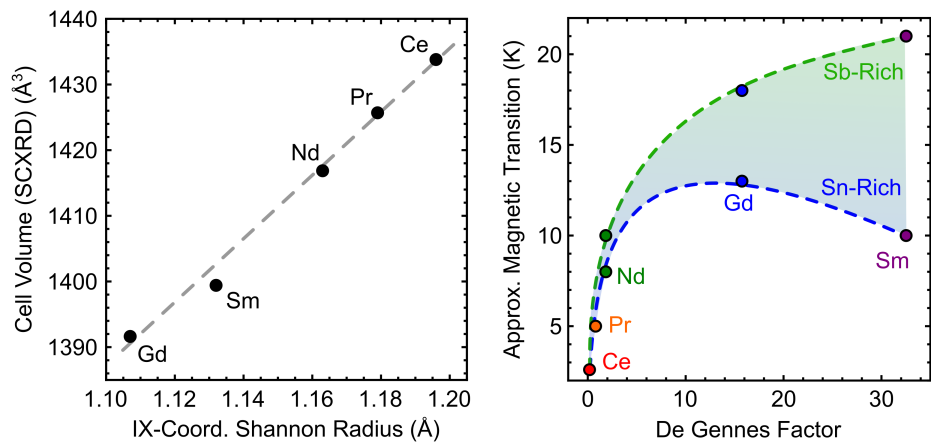


FIG. S9. Supplementary summary plots showing (a) the trend with lattice parameter throughout the rare-earth series, and (b) the De Gennes factor versus the magnetic transition temperatures, where both the Sn-rich and Sb-rich compound are shown for each rare-earth.